



**HAL**  
open science

# Inverse analysis of the impact response of a rockfall protection structure: Application towards warning and survey

Ritesh Gupta, Franck Bourrier, Stéphane Lambert

## ► To cite this version:

Ritesh Gupta, Franck Bourrier, Stéphane Lambert. Inverse analysis of the impact response of a rockfall protection structure: Application towards warning and survey. 2024. hal-04582717v1

**HAL Id: hal-04582717**

**<https://hal.science/hal-04582717v1>**

Preprint submitted on 22 May 2024 (v1), last revised 6 Sep 2024 (v2)

**HAL** is a multi-disciplinary open access archive for the deposit and dissemination of scientific research documents, whether they are published or not. The documents may come from teaching and research institutions in France or abroad, or from public or private research centers.

L'archive ouverte pluridisciplinaire **HAL**, est destinée au dépôt et à la diffusion de documents scientifiques de niveau recherche, publiés ou non, émanant des établissements d'enseignement et de recherche français ou étrangers, des laboratoires publics ou privés.



Distributed under a Creative Commons Attribution 4.0 International License

# Inverse analysis of the impact response of a rockfall protection structure: Application towards warning and survey

Ritesh Gupta<sup>a</sup>, Franck Bourrier<sup>a,b</sup>, Stéphane Lambert<sup>a,\*</sup>

<sup>a</sup>Univ. Grenoble Alpes, INRAE, CNRS, IRD, Grenoble INP, IGE, 38000 Grenoble, France

<sup>b</sup>Univ. Grenoble Alpes, Inria, CNRS, Grenoble INP, Institute of Engineering, LJK, 38000 Grenoble, France

---

## Abstract

The viability of a rockfall protection structure is vital for the hazard mitigation of habitations and infrastructures. This article investigates the feasibility and potential of inverse analysis applied to data collected on on-site rockfall protection structures exposed to real events. As an application case, a rockfall protection wall made from interconnected concrete blocks which are piled up in a zig-zag pattern is considered. The numerical model of this structure is created via the use of a Non-Smooth Contact Dynamics (NSCD) method-based modelling technique. The NSCD model is developed using the SICONOS software and spatiotemporally calibrated from two real-scale impact experiments with 520kJ and 1020kJ projectile energy. This model is used to investigate the variability in wall mechanical response against different impact conditions. The simulation results served as input data for developing the inverse analysis method. As a first application, it is proposed to use the inverse analysis to aid in remote decision-making shortly after an event, based on real-time measurements. Then, the use of inverse analysis to retrieve the impact condition characteristics (energy, location) from data collected after the event is addressed. The proposed approach appeared efficient for back-analysing (*i.e.*, output to input) data related to the wall response for being used as a warning based on its displacement with respect to the protected element at risk and damage to the wall with root mean square errors (RMSE) of 16 cm and 82 kJ respectively and for a rockfall site survey with RMSE of 71 kJ energy transferred to the wall and position of impact with 37 cm.

*Keywords:* rockfall, impact, meta-model, statistical learning, NSCD modelling, inverse analysis

---

\*Corresponding author

Email address: [stephane.lambert@inrae.fr](mailto:stephane.lambert@inrae.fr) (Stéphane Lambert)

## 1. Introduction

Passive rockfall protection mitigation measures such as embankments [1], galleries [2] or flexible barriers [3] are exposed to severe loading when intercepting rock blocks threatening elements at risk. During their normal operation, these structures thus experience significant deformation, displacement, and damage and possibly fail to withstand the impact or to satisfactorily control the rock blocks trajectory [4].

In this context, and similarly, as for other gravitational natural hazards, increasing use is being made of equipment for monitoring on-site rockfall protection structures, to collect the data upon the impact of a rockfall [5]. On-site monitoring of structures with accelerometers or force sensors, for example, in particular aim at serving as a warning system for supporting decision-making (*e.g.*, road closure) or for providing information regarding the loading amplitude or the structure response in real situations. On-site monitoring is becoming increasingly common in the field of landslides due to the improvement, miniaturisation and cost reduction of sensors, data acquisition and transmission systems [6, 7].

Numerical models are widely used for addressing rockfall protection structures' response as a forward problem. Published research demonstrates the accuracy of the model predictions as compared to experimental data (*e.g.* [8, 9, 10]) or addressing the structure response under some specific impact conditions (*e.g.* [11, 12]) or considering sets of realistic impact conditions (*e.g.* [13, 14]). By contrast, inverse analysis conducted (*i.e.*, finding input from the output) based on numerical models have rarely been used in this field. To the best of the authors' knowledge, the only exception concerns the work presented by Escallón et al. [15] who proposed an inverse optimisation process for determining the parameters of macroscopic FE models of steel wire-rope cables and steel wire-rings.

This article investigates the feasibility of conducting an inverse analysis of the structure response for deriving information with added value for stakeholders and engineers. It is for example proposed to analyse the measured data pertinent to the structure's performance to retrieve the impact conditions. The proposed inverse analysis consists of comparing data collected on-site during or after an event with the structure impact response as obtained from numerical simulations. This comparison relies on the use of statistical learning methods enhanced by meta-modelling tools. A statistically modelled series of different impact conditions and a learning-enabled link between input and output responses provide us with the necessary components to do the inverse analysis. Further, the establishment of a mathematical link between the structure's response and the corresponding impact condition is enabled through the use

30 of meta-models having negligible computation costs.

31 Here, we focus on an innovative passive rockfall protection structure made of pile-up concrete blocks  
32 to form a wall with a zig-zag pattern, for which a Non-Smooth Contact Dynamics (NSCD) method-based  
33 numerical model was previously developed. The calibration of this model was conducted against experi-  
34 mental data following a complex method involving statistical learning, resulting in improved confidence in  
35 the model's predictive capacities, reported in [16]. In parallel, specific instrumentation including sensors  
36 (*i.e.* accelerometers and inclinometers), remote data acquisition and processing has been developed to  
37 equip these structures. In principle, the proposed approach for conducting an inverse analysis could be  
38 applied to any type of structure, and in particular structures exposed to dynamic loading such as flexible  
39 barriers.

40 The paper is organised as follows: First, the NSCD model definition and its calibration are briefly  
41 presented. Then the mechanical response of the wall to impact is addressed thanks to NSCD model  
42 simulations. First, varying the impact location and then via six parameters collectively describing the  
43 rock block trajectory, kinematics and impact point on the wall. The impact simulation results highlight  
44 the intricacy of the structure response and suggest the simulation outputs which best allow differentiating  
45 the impact cases. Then, a method for conducting the inverse analysis of the collected data is developed  
46 to support the real-time decision and rockfall activity monitoring purpose of a given site.

## 47 **2. Structure and model presentation**

48 The considered structure is a composition of concrete blocks, reinforced with internal rebars and placed  
49 together in a staggered pattern to form a wall whose geometry can be adapted to specific requirements  
50 (e.g. linear or zig-zag conformation along its longitudinal axis). The blocks are connected thanks to  
51 metallic tubes and cables passing through vertical cylindrical holes in the blocks, providing mechanical  
52 continuity to the structure [17]. There exist mechanical plays between concrete blocks of the same row  
53 as well as between the metallic tubes and the blocks.

54 This type of articulated structure constitutes an alternative to other massive passive rockfall protection  
55 structures with reduced footprint [18, 19] with the advantages of high versatility in the design and  
56 deformability under impact. For such an application where the structure is exposed to a localised dynamic  
57 loading, tubes and cables increase the number of blocks involved in the structure's response proportional

58 to the impact loading.

59 The dynamic response of this structure is evaluated thanks to two full-scale impact experiments with  
60 energies of 520kJ and 1020kJ on a wall 3.2 m in height and 14.1 m in length (Figure 1a). The projectile  
61 used for this purpose is 2600kg in mass and 1.1 m in dimension, corresponding to approximately  $1/3^{rd}$   
62 the wall height, conforming with the requirements of flexible barrier testing [20]. The wall displacement  
63 evolution data is recorded at a couple of points on the impact axis (at points Top and Base) and on the  
64 distant axis (at points C and D) as further detailed in Furet et al. [17].

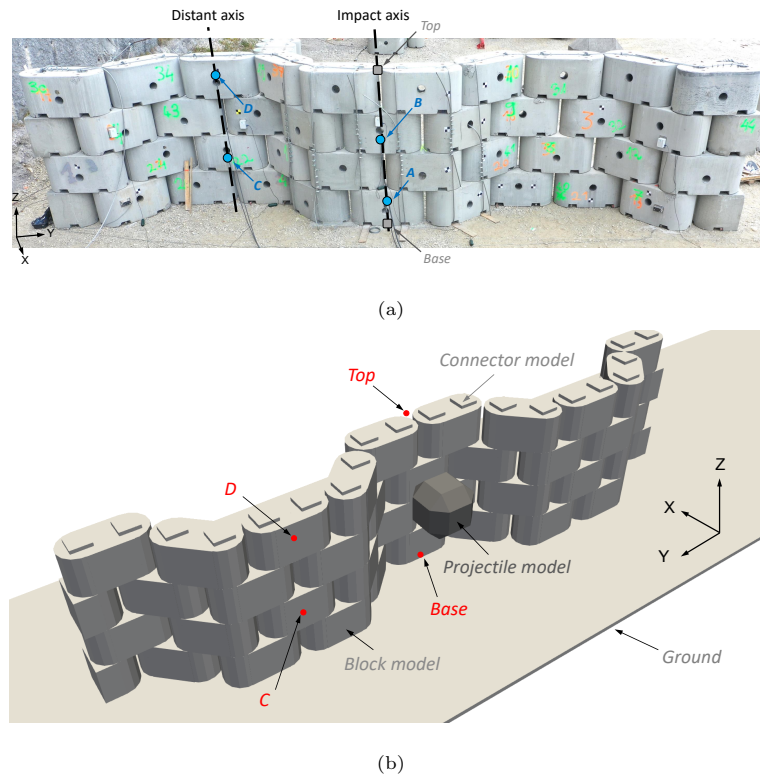


Figure 1: (a) The experimental real-scale wall structure and (b) its numerical equivalent developed using SICONOS software based on the framework of non-smooth contact dynamics (NSCD) method, hereby referred to as NSCD model.

65 Based on these impact experiments, a numerical model of the structure was developed under the  
66 Non-Smooth Contact Dynamics (NSCD) framework implemented in SICONOS [21] software. The NSCD  
67 model of the structure is a collection of blocks and connectors (Figure 1b). The detailed description of  
68 the model development and calibration is presented in Gupta et al. [16].

69 The same block geometry is considered in the model as that in the real structure. The cables and  
70 slings are modelled with connectors. The interaction between the structure model components, as well  
71 as the interaction with the projectile, abides with the framework of the NSCD method.

72 The model parameters governing the interactions between the various bodies of the system were  
73 calibrated against the experimental database describing the spatio-temporal response of the wall during  
74 the two impact tests. Notably, the calibration was based on the displacement measured with time (at  
75 three-time instants) at the four locations previously mentioned. The model calibration was supported by  
76 the Bayesian statistical learning method, improving the confidence in the derived set of model parameters,  
77 and thereby enabling the replication of the structure response with time and space, over a range of  
78 impact energies up to 1 MJ. In addition, the model being simple and developed under the NSCD method  
79 framework provides on average about 30 times faster computation times in comparison to conventional  
80 FE-based models [17] and allows envisaging running a large number of computations.

81 In the following, all simulations are conducted on a wall 3.2m high and about 28.2m long (Fig. 2).  
82 The increase in length as compared to that in Gupta et al. [16] aims at avoiding any potential boundary  
83 effects when varying the impact location along the wall longitudinal axis. For these simulations, the same  
84 projectile is considered. Moreover, the comparison of spatio-temporal displacement response for both  
85 small and large wall lengths (*i.e.*, 14.1 and 28.2m respectively) for the two calibrated impact cases are  
86 reported qualitatively and quantitatively similar. Therefore, the calibrated model constitution parameters  
87 as reported in Gupta et al. [16] are directly applied to the long wall model.

### 88 3. Structure response investigation

89 Due to its zig-zag conformation, discrete nature and complex design where concrete blocks are in-  
90 terconnected thanks to metallic components and including mechanical plays, the structure response is  
91 expected to be highly sensitive to impact conditions, for example varying the impact location or the  
92 projectile pre-impact trajectory.

93 First, the structural response variability is illustrated by considering three impact cases in similar  
94 conditions to that during the experiments but with different impact locations. Then the investigation is  
95 generalised varying 6 parameters describing the impact conditions.

#### 96 3.1. Response for the illustrative impact conditions

97 The wall response is addressed by varying the projectile impact location to illustrate its complexity  
98 and variability. Three impacts with a 520 kJ energy and located in the centre of each of the distinct

99 sections of the zig-zag pattern were simulated. These sections are referred to as convex-wedge, angled-  
 100 wedge and concave-wedge, when viewed from the impacted side, as presented in Figure 2. The wall  
 101 response is addressed in terms of block displacement, velocity, inclination and plastic damage.

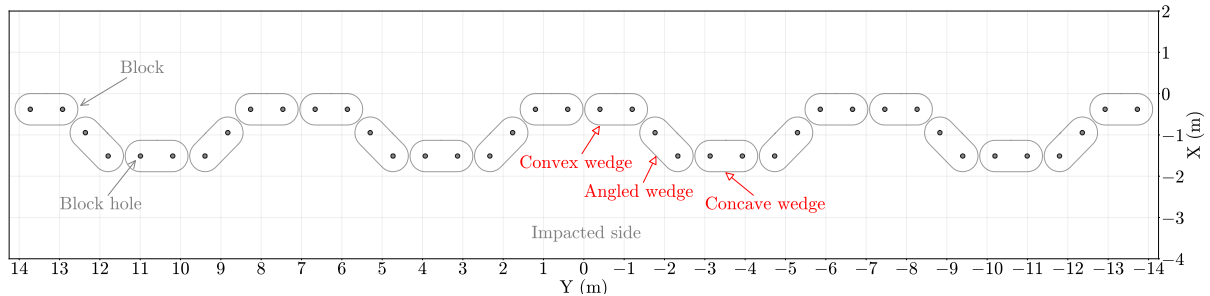
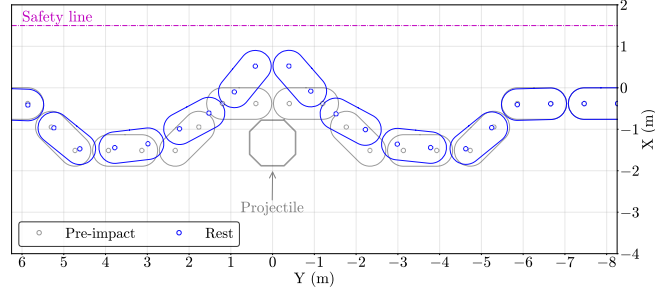


Figure 2: Top view of the wall model highlighting the repetitive pattern and an identifier for different sections.

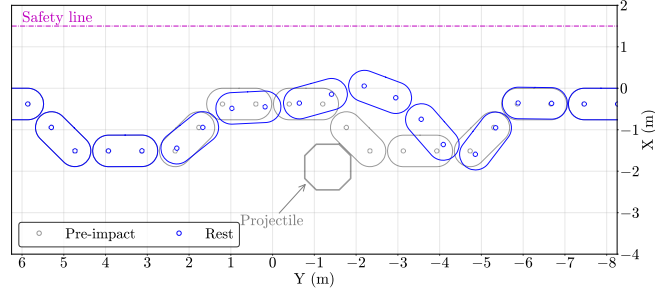
### 102 3.1.1. Displacement

103 The displacement at the top of the wall is extremely sensitive to the impact location, presented for  
 104 three illustrative impact conditions (IC), via the top view of the wall in Figure 3. Here, the three simulated  
 105 impacts one each at convex, angled and concave wedges are named as IC-1, IC-2 and IC-3 respectively.  
 106 This is particularly noticeable in terms of structure conformation. The impact on the concave-wedge  
 107 results in aligned blocks (Fig. 3c), while an impact on the convex-wedge amplifies the amplitude of  
 108 the zig-zag (Fig. 3a). The length of the movement zone along the wall longitudinal axis varies from  
 109 approximately 6 m in the case of an impact on the angled-wedge to 7 m for the two other impact cases,  
 110 corresponding to four and six number of top-row blocks respectively. Figure 3 also suggests a difference  
 111 in the displacement of the individual blocks. Larger block displacement is observed for impacts on the  
 112 concave-wedge.

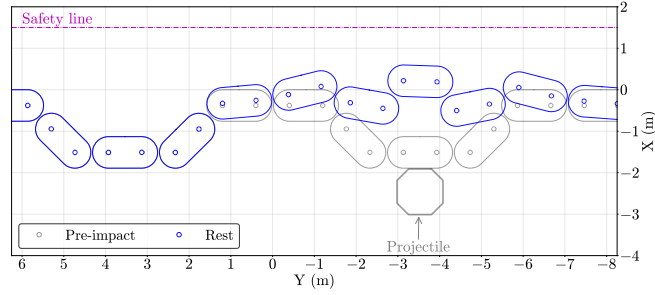
113 As this zig-zag patterned wall aims at protecting a given element at risk it appears much more  
 114 relevant to consider the residual distance to the so-called safety line shown in Figure 3 in addition to of  
 115 the displacement of the blocks. The safety line may be defined based on the position of the protected  
 116 element at risk. It is here arbitrarily located at 1.5 m from the convex-wedge block's rear face. From  
 117 Figure 3, it can be deduced that the minimum residual distance to the safety line is much smaller in the  
 118 case of the impact in the convex-wedge (0.5 m. approx.), as compared to the two other impact cases (1.3  
 119 m approx.). With respect to this criterion, an impact on the convex-wedge thus reveals comparatively  
 120 more critical than others.



(a)



(b)



(c)

Figure 3: Top view of the structure before and after a 520-kJ impact located in the centre of (a) the convex-wedge (IC-1), (b) the angled-wedge (IC-2) and (c) the concave-wedge (IC-3).

### 121 3.1.2. Velocity

122 The variability in response is here illustrated by the time evolution of the velocity of the concrete  
 123 blocks. For this purpose, the velocity computed at the mid-bottom of the block rear vertical face ' $v_{\text{face}}$ '  
 124 (*i.e.*, on the side opposite to impact) is considered which represents the potential position for the sensor  
 125 deployment in the in-situ structure.

126 Instrumentation of on-site structures is likely to consist of 1D accelerometers installed on the concrete  
 127 block faces for measuring the acceleration normal to the block with time. For a simplified analysis, the  
 128 desired velocity profile from the NSCD model shall also be computed normal to the block face at all time  
 129 instances. For this, the ' $v_{\text{face}}$ ' vector is projected onto the unit normal vector ( $\hat{n}_b$ ) to the block face. The  
 130 computation process is presented in Equation 1.



$$v_{\text{face}} = v_{\mathbf{g}} + (p\Omega p^{-1}) \times q \quad (1)$$

$$v_{\text{nb}} = (v_{\text{face}} \cdot \hat{n}_{\mathbf{b}}) \hat{n}_{\mathbf{b}}$$

131 where  $v_{\mathbf{g}}$  is the velocity at the block gravity centre,  $\Omega$  is the rotational velocity,  $p$  is the quaternion  
 132 (presenting block's 3D orientation) and  $q$  is the relative position vector of the block face (envisaged sensor  
 133 location) to its centre of gravity.

134 The time evolution of velocity normal to block face computed for all three cases is presented in  
 135 Figure 4 (all left). In addition, the peak velocity of the blocks and the time to reach this peak are plotted  
 136 in Figure 4 (all right).

137 A general trend where the peak velocity localises at the impacted block is observed. Besides, the  
 138 number of blocks experiencing rapid displacement from the impact beginning is comparatively higher  
 139 when the projectile impacts the concave-wedge (Fig. 4c). Indeed, three blocks close to the impact location  
 140 experience very similar curves. The time for the wall to come to rest is smaller in case of an impact on  
 141 the convex-wedge with a duration of about 0.5 as compared to 0.8 seconds after an impact on the angled-  
 142 wedge in particular (Fig. 4a vs Fig. 4b). Overall, the velocity of all the blocks appears to provide rich  
 143 information, with high amplitude as well as significant differences from one case to the other.

144 The blocks with significant maximum velocities are located within a distance along the wall length  
 145 ranging from 8 to 12 m approximately depending on the impact location. This observation is in line with  
 146 the observation made in Figure 3. The shape of the maximum velocity pattern significantly differs from  
 147 one impact case to the other. These observations suggest that the distribution of peak velocity along the  
 148 wall could be specific to the impact case in a rather univocal manner.

### 149 3.1.3. Inclination

150 In addition to the displacement and velocity, the inclination of the wall blocks, *i.e.*, their rotation  
 151 around a horizontal axis, seems relevant to address as it relates to wall post-impact stability. In addition,  
 152 inclination may be measured on-site with rather low-cost sensors. The post-impact inclination of all the  
 153 blocks in the wall is presented in Figure 5. An impact on the concave-wedge results in block inclination  
 154 over a wall length as large as 8 m (Fig. 5). The maximum value of about 17° approx. is observed at the  
 155 upper row in the impact vicinity. Results concerning the impact on the convex-wedge and angled-wedge  
 156 are not presented as they induced nearly zero wall inclination.

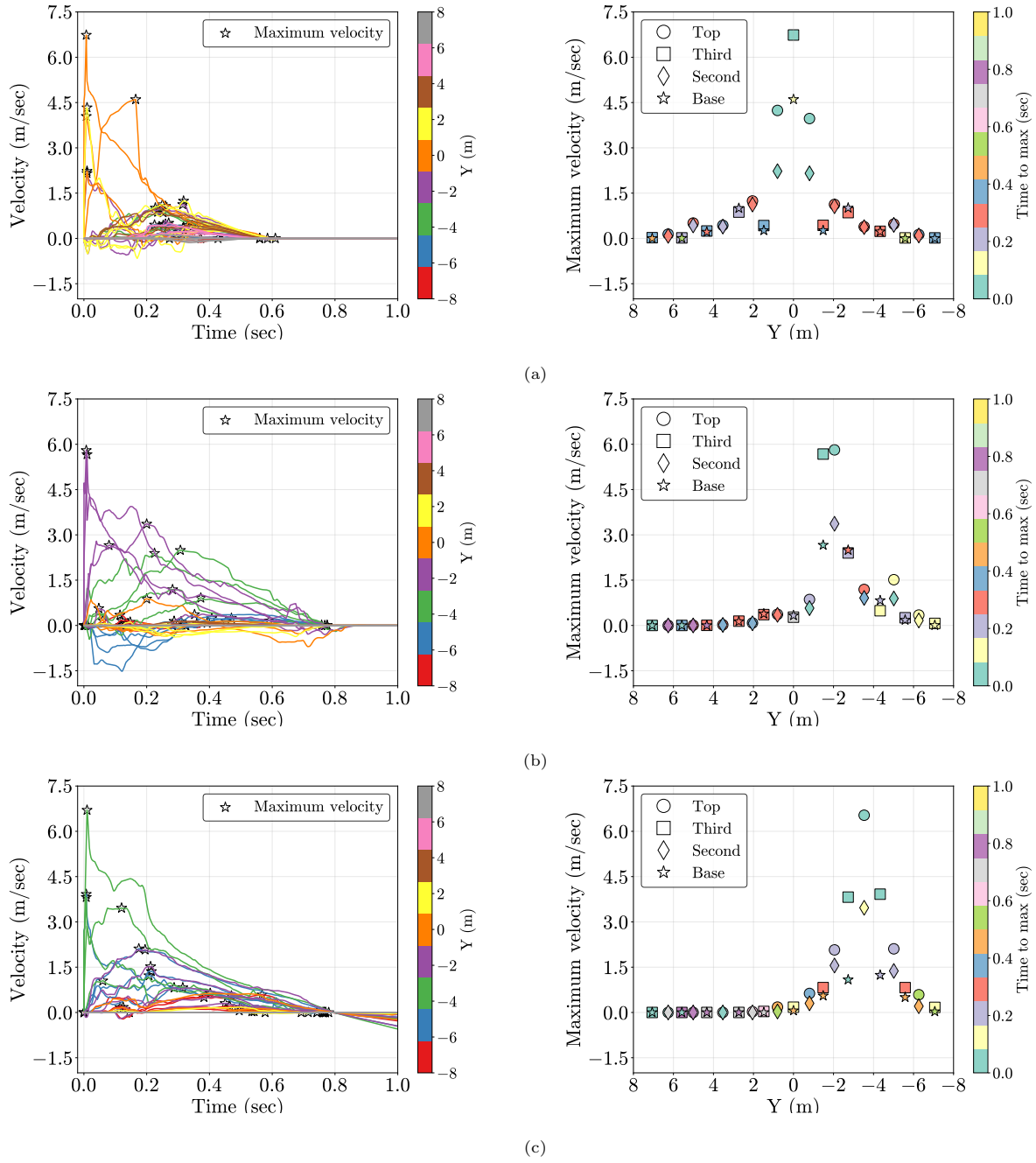


Figure 4: Evolution of the velocity of the concrete block in the movement zone (all left) and the corresponding mapping of the maximum velocity for blocks in all four rows *i.e.*, top, third, second and base (all right) for the illustrative impact cases at (a) convex wedge (IC-1), (b) angled wedge (IC-2) and concave wedge (IC-3) respectively. Here, ‘Y’ refers to the global position of the mid-bottom of the rear face of each block along the wall length.

157 Conclusively, the inclination doesn’t provide sufficiently rich information to envisage relating it to the  
 158 impact conditions, in particular, because some impact conditions result in null inclination angle values  
 159 and hence are not deemed appropriate to explore further.

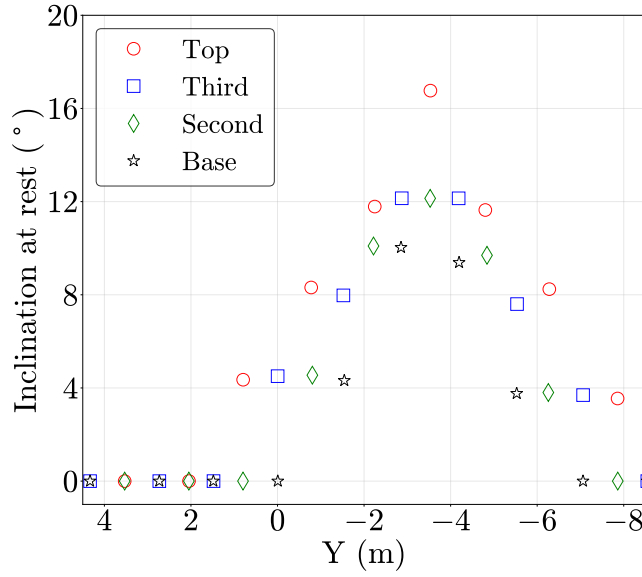


Figure 5: Inclination of all blocks in four layers of the wall (*i.e.*, top, third, second and base) with respect to the vertical at rest for the impacts at concave wedge (IC-3) under 520kJ energy impact. The results for the impact at the convex-wedge (IC-1) and angled-wedge (IC-2) are not presented because of their negligible magnitude.

### 160 3.1.4. Plastic damage

161 The rockfall impact on the structure causes plastic damage to the blocks, dissipating a portion of the  
162 incident projectile kinetic energy. Notably, the NSCD model is created as an accumulation of rigid bodies  
163 where the contact law controls the interaction. Despite that, the quantitative estimation of the energy  
164 dissipation mechanisms is possible following the work reported by Acary [22] in the NSCD framework.  
165 Subsequently, the relation presented in Equation 2 is implemented in the present work to compute the  
166 energy dissipation due to plasticization ( $D_p$ ).

$$D_p = \sum_{k=0}^N \sum_{\alpha \in I} \frac{1}{2} (v_{N,k+1}^\alpha + v_{N,k}^\alpha) P_{N,k+1}^\alpha \quad (2)$$

167 Here,  $v_N$  is the normal component of the velocity vector and  $P_N$  is the normal impulse at a given time  
168 step ' $k$ ' (out of total  $N$ ) at a contact point  $\alpha \in I$ . The details of velocity and impulse computations can  
169 be referred to at Gupta et al. [16].

170 The time evolution of  $D_p$  for the three illustrative cases with different impact locations is presented  
171 in Figure 6. A significant contribution of plastic damage is observed at the early time instance when  
172 the projectile impacts the wall. With reference to the zoomed-in window (see Figure 6b), the damage  
173 evolves relatively fast for the impact at convex-wedge (IC-1) and reaches a constant magnitude of about

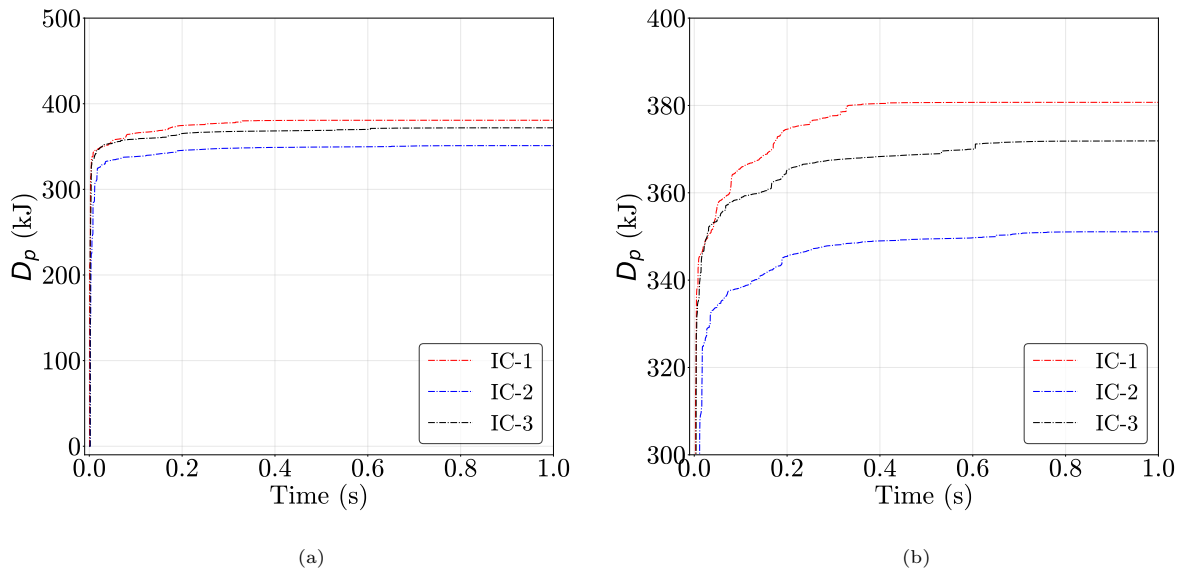


Figure 6: (a) Time evolution of the energy dissipation due to plastic damage for the three illustrative cases, with impact at at the convex-wedge (IC-1), the angled-wedge (IC-2) and concave-wedge (IC-3), (b) zoom-in window between 300 and 400 kJ

174 380kJ at about 0.35 seconds post-impact. The other two impact cases evolve for a relatively longer time  
 175 (about 0.6 seconds) before reaching a constant value. This observation is in line with the duration over  
 176 which the wall moves, as illustrated in Figure 4. Conclusively, the plastic damage is taken as a quantity  
 177 of interest for structural response assessment.

178 Notably, the remaining part of the energy transferred by the projectile to the wall is dissipated by  
 179 friction at the contacts, as detailed in [23] where it is also demonstrated that the computation scheme  
 180 complies with the fundamental principle of energy conservation.

### 181 3.2. Response to a large set of impact conditions

182 Following the illustrative structural response description in the previous section, the numerical sim-  
 183 ulation framework is extended to address the response considering a large set of impact conditions. In  
 184 a similar way as previously done for flexible barriers [13, 24, 25], the parameters describing the incident  
 185 projectile trajectory, kinematics and location, hereafter referred to as ICPs (Impact Conditions Param-  
 186 eters) are varied over realistic ranges to account for nearly all possible distinct impact conditions which  
 187 may occur in the field. The ICPs and their magnitude ranges are given in Table 1.

188 The first two parameters (*i.e.*, translational and rotational velocities) account for the incident kinetic  
 189 energy of the projectile. Given the projectile geometric and mechanical characteristics considered in this

Table 1: Parameters considered for generating close-to-reality impact conditions

Parameter	Possible range	Distribution	Unit
Translational velocity ( $v$ )	10 - 25	Gaussian	m/s
Rotational velocity ( $\Omega$ )	0.0 - 5.6	Uniform	rot/sec
Impact position - along length (offset) ( $y$ )	0.0 - -3.53	Uniform	m
Impact position - along wall height ( $z$ )	0.55 - 2.10	Uniform	m
Impact inclination ( $\alpha$ )	-60 - +60	Uniform	$^{\circ}$
Impact deviation ( $\beta$ )	-45 - +45	Gaussian	$^{\circ}$

190 study, the translation velocity results in a kinetic energy ranging from 130kJ to 800 kJ. The rotational  
 191 velocity range is defined as per the work reported by Bourrier et al. [26] providing the rotational kinetic  
 192 energy up to 240kJ for the projectile geometry used in this work.

193 The impact location refers to the projectile's centre of gravity at impact. The range for the impact  
 194 locations along the wall longitudinal axis (Y axis) is defined considering that the structure consists of the  
 195 repetition of a pattern. Thereby, the impact locations were restricted to a representative segment of the  
 196 wall conformation. By definition, the response observed for this segment is extendable to other parts of  
 197 the wall, except for the wall extremities. Indeed, impacts at a close distance from the wall extremities  
 198 shall result in a different impact response, in particular depending on some design choice with influence  
 199 on the mobility of the blocks at the wall extremity (such as retaining cables or abutments). The case  
 200 of impacts close to the wall extremities is thus not considered in the present work. The impact location  
 201 along the vertical axis ( $z$ ) is defined considering the wall height and the block size, which is 1.1m. The  
 202 minimum value for the impact location along the vertical axis is half the projectile dimension. The  
 203 maximum value corresponds to the distance between the projectile centre of gravity and the wall crest  
 204 equalling the projectile diameter.

205 The inclination and deviation angles are varied over the ranges reported by Toe et al. [24]. The  
 206 inclination angle ( $\alpha$ ) represents the relation of the z-component of projectile impact path with the normal  
 207 to the wall face [13]. Negative  $\alpha$  values thus correspond to upward trajectories (*i.e.*, away from the  
 208 ground). The  $\beta$  angle accounts for the deviation in the horizontal plane of the incident rock block

209 trajectory with respect to the normal to the wall longitudinal axis (and not with respect to the impacted  
210 block uphill face). The range considered for  $\beta$  implies that the wall longitudinal axis is considered  
211 perpendicular to the line of the maximum gradient of the uphill slope.

212 In this study, the kinetic energy is considered sufficient for describing the projectile kinematics in view  
213 of addressing the structure response. This obviously constitutes a simplification as it is evidenced that,  
214 for a given projectile kinetic energy, the response of a rockfall protection structure may be significantly  
215 influenced by the projectile mass-to-velocity ratio [27, 28]. Besides, the upper limit of the translational  
216 kinetic energy is kept less than the wall nominal capacity as observed during the experiments, which is  
217 above 1 MJ. This is motivated by two observations: (1) The representation of the model to correctly  
218 model the structure displacement and damage is lower at impact kinetic close to the nominal value (*e.g.*,  
219 due to loss of mechanical continuity in connectors [16]) and (2) The damage and displacement are severe  
220 for translational kinetic energy at impact higher than 800 kJ, imposing visit and repair/maintenance  
221 works without any doubts.

### 222 3.2.1. Statistical sample

223 A statistical set of 300 model computations, based on the Latin hypercube sampling (LHS) method  
224 [29] is retrieved to represent the model response under multiple impact conditions. The created statistical  
225 sample is presented in Figure 7. Here, the filled input space assures that possible combinations of the  
226 input variables are well considered in the finite set of ICPs.

227 It is worth highlighting that the ICPs were defined ignoring some correlations that may exist between  
228 the six parameters. For example, the velocity in the case of a downward projectile trajectory is higher  
229 on average than that for an upward trajectory. This results from the fact that a downward trajectory  
230 is associated with a rock block-free fall while an upward projectile trajectory immediately succeeds in a  
231 rebound in the ditch which induces energy dissipation. This means that some combinations of parameter  
232 values are not realistic (for example the lowest  $\alpha$  value with the highest translational velocity,  $v$ ).

233 Moreover, a probability distribution is assigned to each parameter to account for the influence of rock-  
234 fall trajectory, as suggested in Lambert et al. [14]. A Gaussian distribution is chosen for the translational  
235 velocity ( $v$ ) and deviation angle ( $\beta$ ) indicating that the extreme limits of both these parameters are less  
236 probable. The parameter  $\beta$  distribution abides by the idea that the structure installation on site is such  
237 that the projectile is most likely to impact normally to its face. Similarly, the parameter  $v$  distribution

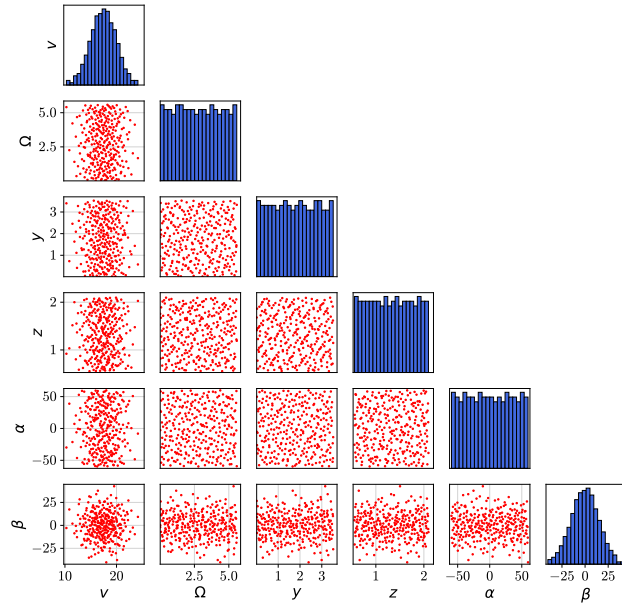


Figure 7: Input sample of size 300 (based on Latin hypercube sampling (LHS) sampling method) comprising six impact condition parameters (ICPs) and their probability distribution in the respective ranges of variability.

238 takes into account the most likely impacting projectile energy and keeps the low and high energy cases as  
 239 rare events. The uniform distribution is assigned for all the remaining parameters as no prior information  
 240 is available on their probability of occurrence.

### 241 3.2.2. Displacements under impact

242 The position of the top row blocks at the end of impact (*i.e.*, at rest) for all 300 simulations is  
 243 presented in Figure 8. The hollow circles correspond to the location of the extremity of the vertical  
 244 connectors position. The blocks represented in blue correspond to the impact case resulting in the least  
 245 distance from the wall to the safety line. Impacts in the convex-wedge resulted in a lower distance to  
 246 the safety line which is consistent with observations made based on Figure 3. The movement zone for  
 247 all simulated cases stays within approximately 7m on either side from the centre of the wall (*i.e.*,  $Y =$   
 248  $0$ ). The cloud of points, together with the mean positions and the variability (estimated as twice the  
 249 standard deviation), reveals that the amplitude of the displacement in the X- and Y-axis directions are  
 250 much larger at a distance from the wall centre (*i.e.* at the concave wedge) and that it is significantly  
 251 dependent on the impact location along the Y-axis.

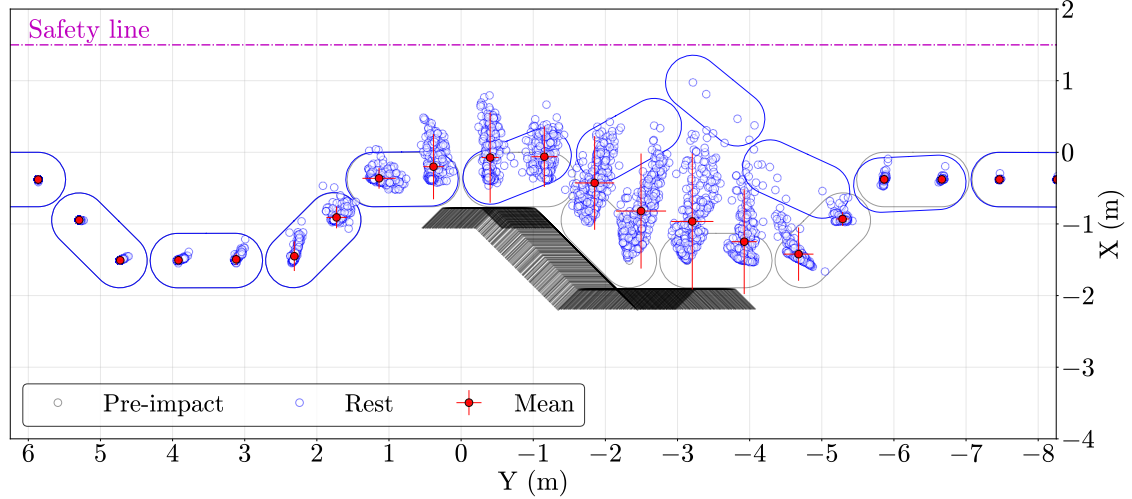


Figure 8: Displacement of the wall's top row blocks under 300 sampled impact conditions. The position of the blocks holes position after impact is presented for each simulation and the impact case resulting in the least distance to the safety line is highlighted for better visibility.

### 252 3.2.3. Sensitivity analysis

253 The variability in structure response is further addressed by investigating the influence of each pa-  
 254 rameter on the different quantities of interest (QoI). In accordance with Section 3.1, the considered QoIs  
 255 are the minimum distance to the safety line ( $u^{safety}$ ), the maximum displacement of the wall ( $u_{max}$ ), the  
 256 maximum concrete block velocity recorded ( $v_{max}$ ) during impact and plastic damage ( $D_p$ ).

257 The influence of each parameter on the QoIs is investigated through the Sobol sensitivity method also  
 258 known as analysis of variance [30]. This method decomposes the variance of the output parameters as  
 259 the sum of the contributions of the different input parameters including the possible interaction between  
 260 input parameters. Each contribution is characterised by the ratios of the partial variance to the total  
 261 variance, called Sobol sensitivity indices.

262 The accurate computation of Sobol indices demands a large number of model computations (of order  
 263  $10^6$ ). This is highly impractical in the present study if the NSCD model is used directly. This limitation  
 264 is circumvented with the help of the meta-modelling technique which enables to create a surrogate of the  
 265 NSCD model, allowing direct computation of Sobol indices at a highly reduced cost [31, 32]. In this case,  
 266 a meta-model (or surrogate) can be defined as a mathematical operator describing the response envelope  
 267 of the wall in the 6D space corresponding to the six variables defining the impact conditions related to  
 268 the rock projectile.

269 Here, a database of 300 model simulations is processed for each QoI to acquire the model output set and



its corresponding ICPs. Then, the polynomial chaos expansion (PCE) based meta-modelling technique (as per UQlab PCE module [33], see Appendix A for details) is used to formulate a generalised link between the input ICPs and the output QoI. For each meta-model creation, a mathematical relation (as presented in Equation A.2), is established between the 300 distinct sets of input parameters and the corresponding displacement output set. The mathematical relation here can be analogically referred to as obtaining a regression for a 2D database. The accuracy of the PCE-based meta-model is presented by the leave-one-out (LOO) error (Equation A.5), reported of order  $10^{-2}$  for  $u^{safety}$ ,  $u_{max}$  and  $D_p$  and of order  $10^{-1}$  for  $v_{max}$ .

The UQlab sensitivity analysis module [34] is used for such computations. The first and total order Sobol indices for the QoI are presented in Figure 9. The Sobol indices are computed to evaluate the influence of each of the six ICPs on the four aforementioned QoI.

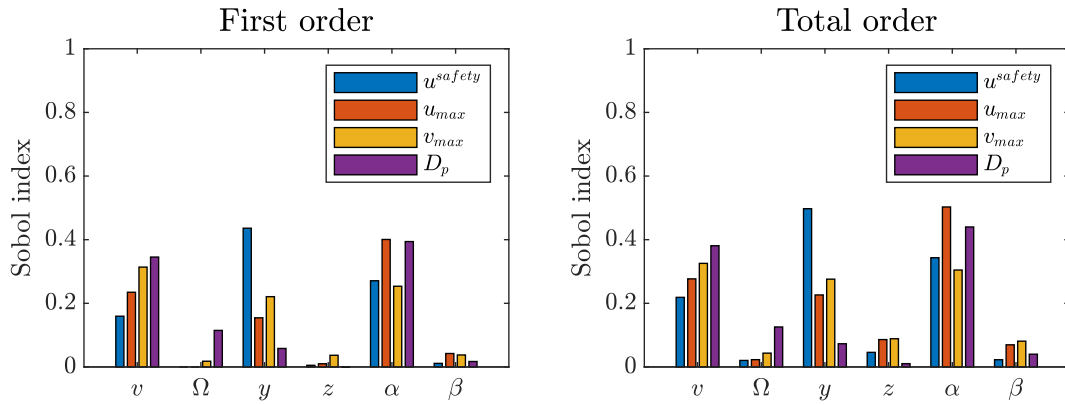


Figure 9: Sobol sensitivity analysis of the ICPs on different QoI towards the representation of the generalised impact assessment.

The first-order Sobol indices reflect the main effect of each ICP and the total order indices reflect the main effect inclusive of the contribution from the interaction between different ICPs. When there is no interaction between variables, the first and total index magnitudes shall be the same. However, the contrary is observed here which reflects the significant interaction between ICPs in terms of their influence on the QoIs.

Moreover, the main effect of the rotational velocity (except for  $D_p$ ), the vertical position of impact ( $z$ ) and deviation ( $\beta$ ) are observed to have the lowest sensitivity to all QoIs. On the contrary, all QoIs are reported to be highly sensitive to the other three input ICPs. The  $y$  position of projectile impact is observed to be highly influential confirming the structural response variability from convex to angled to

290 concave wedges, as reported in Figures 3 and 8.

291 The  $v$  and  $\alpha$  parameters collectively account for the projectile velocity component parallel to the  
292 ground (xy plane) and the component parallel to the wall face (z-axis) as presented in Equation 3.

$$\begin{aligned}v_z &= v \sin \alpha \\v_{xy} &= v \cos \alpha\end{aligned}\tag{3}$$

$$v_x = v_{xy} \cos \beta, \quad v_y = v_{xy} \sin \beta$$

293 It is thus evident that these three input ICPs control all resulting QoI directly. Notably, the parameter  
294  $\beta$  determines the further division of projectile velocity ( $v$ ) in x-y plane (*i.e.*,  $v_x$  and  $v_y$ ). Since  $\beta$  is observed  
295 to have a low influence on the QoI, the collective effect of projectile velocity in xy-plane is sufficient for  
296 further consideration.

### 297 3.3. Towards inverse analysis

298 The investigation of the structure response under close-to-reality conditions is of paramount impor-  
299 tance, first, for evaluating its on-site efficiency and, second, for defining the best strategy for developing  
300 the inverse analysis method.

301 The wall response to impact is revealed extremely complex, with a significant dependence on pa-  
302 rameters describing the impact conditions (ICPs). Differences in response were revealed by the concrete  
303 blocks' kinematics, in terms of displacement and velocity. The sensitivity to the impact point location  
304 along the wall's longitudinal axis results from the wall's zig-zag conformation and its discrete and artic-  
305 ulated nature. In the case of an impact with a zero deviation and at a 520 kJ impact energy, the length  
306 of the wall experiencing significant displacement is up to 12m. This is confirmed by the distinct patterns  
307 of the peak concrete block velocity along the wall (*e.g.*, see Figure 4). In addition, the wall response  
308 depends on the projectile orientation with respect to the wall face ( $\alpha$  and  $\beta$ ) which is attributed to the  
309 amount of energy that is transferred to the wall during impact (which will be further addressed in see  
310 section 5.2).

311 The complexity of this response justified considering a specific approach for developing a relevant  
312 inverse analysis method. In addition, it is concluded that the inclination of the wall is not relevant for  
313 conducting an inverse analysis. On the contrary, the distribution of the concrete block's peak velocity  
314 seemed to be impact-conditions-specific and is thus considered a good input data candidate for conducting

315 inverse analysis based on real-time measurements made on-site. These conclusions suggest that the  
316 priority in terms of on-site structure instrumentation should be placed on accelerometers, from which  
317 the concrete block velocity can be derived. By contrast, it is less relevant to install inclinometers for the  
318 purpose of conducting inverse analysis.

319 In this work, it is proposed to conduct inverse analysis based on real-time measurements, during  
320 impact, for the purpose of warning and decision-making upon impact. This requires installing sensors  
321 in different locations on the structure, connected to data acquisition and transfer equipment. Then, it is  
322 also proposed to conduct inverse analysis based on data collected on the structure after impact, such as  
323 a cloud of points revealing the structure envelope obtained from scanning tools. These data sets may be  
324 used for conducting post-impact inverse analysis in view, for example, of quantifying the consequence of  
325 the impact on the structure or retrieving information related to the event.

326 In both cases, the inverse analysis basically consists of exploiting the data collected on-site to statis-  
327 tically establish a link with the various impact conditions. The inverse analysis relies on meta-models  
328 created based on a large set of NSCD model simulations of the structure response under close-to-reality  
329 conditions. The Bayesian interface statistical learning method is used where the data collected on-site  
330 shall be fed as evidence into the meta-models based forward model to find out the likelihood of obtaining  
331 the same result (a single value or a pattern) from a particular set of input parameters. A brief descrip-  
332 tion of the Bayesian interface is presented in [Appendix B](#) and its implementation in the present work is  
333 detailed in section [4.2](#).

## 334 **4. Inverse analysis based on real-time measurements**

### 335 *4.1. General considerations*

336 The instrumented protective structures *e.g.*, installed sensors, most often aim at warning the structure  
337 owner or the protected infrastructure manager of any event. Real-time measurements could also be used  
338 to improve decision-making over the next few moments after impact. Such a process could be based on  
339 images from cameras, but sensors have the advantage of providing reliable information independently of  
340 the light and scene conditions.

341 Two decisions could be taken remotely immediately after an impact on a structure protecting a traffic  
342 line: traffic interruption and the need for a structure inspection. Both are related to the consequences of

343 the impact on the structure, in terms of displacement and damage. An excess in one of these latter may  
344 be critical to the safety of the traffic line or imply rapid repair or maintenance work. In this objective,  
345 the inverse analysis is intended to rapidly and remotely provide an indication on the magnitude of the  
346 consequences of the impact, for example using consequence classes, rather than to provide a precise value  
347 of the displacement or damage.

348 The inverse analysis is based on measurements retrieved from the on-site structure. The devices used  
349 for these measurements should consider cost constraints to be of interest in an operational context. In  
350 particular, the number and type of sensors should be optimised. The previous section suggested that a  
351 reliable inverse analysis could be conducted from the block velocity, which can be derived from the on-site  
352 acceleration measurements recorded during the impact. Based on this, the proposed inverse analysis is  
353 developed considering acceleration measurements from uniaxial sensors, because of their much lower cost  
354 compared to triaxial ones. Also, it is developed to constrain the number of required data, meaning the  
355 number of measuring points on the structure (*i.e.*, sensors). The number of measuring points is kept at  
356 a minimum while allowing a sufficiently good prediction accuracy of the inverse analysis.

357 In this perspective, the sensor deployment scheme is defined for a representative wall length, in such a  
358 manner it can be replicated along the full wall length. Considering the minimum length of the movement  
359 zone observed in Figure 4, the choice is made to have at least 3 sensors per wall segment. More precisely,  
360 sensors shall be located in the centre of the vertical face of concrete blocks experiencing significant  
361 displacements whatever the ICPs. This number of sensors per representative length is presumed to be the  
362 minimum number for allowing a reliable inverse analysis. It corresponds to 6 concrete blocks equipped  
363 with sensors over the maximum movement zone length, as shown in Figure 10. Here, the illustrative  
364 process of acceleration data acquisition followed by its integration to obtain velocity evolution with time  
365 for each sensor is also presented. The maximum velocity magnitude is identified and consequently, the  
366 pattern of maximum velocity for each sensor processed data is retrieved which is deemed unique for each  
367 impact condition.

368 The inverse analyses presented in the following make use of the maximum concrete block velocity  
369 along the direction normal to the block face at these 6 locations. The set of maximum block velocities  
370 recorded along the wall at these locations is in the following referred to as the maximum velocity pattern  
371 (MVP).

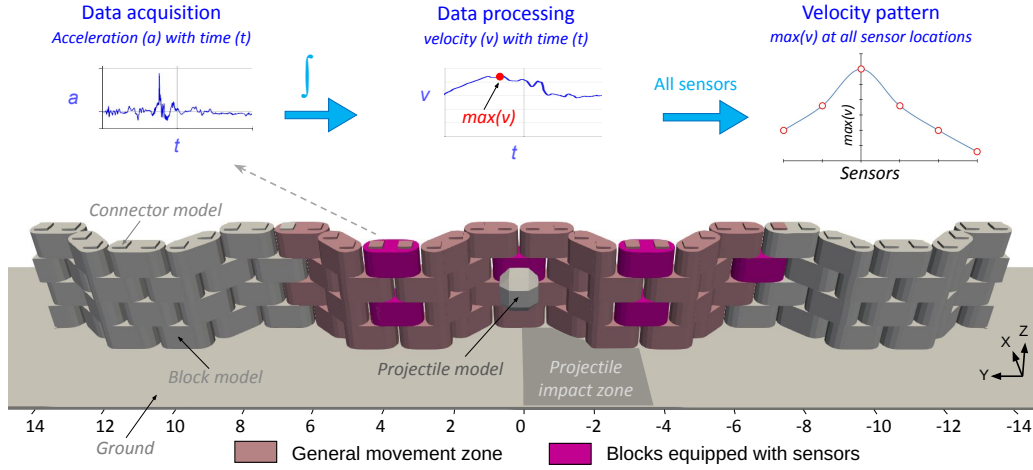


Figure 10: The schematics of the wall model where some blocks are equipped with sensors for data acquisition

372 *4.2. Inverse analysis method*

373 The inverse analysis relied on the confrontation between the MVP obtained from on-site measurements  
 374 to that obtained from a large number of simulation-based results. The developed method for conducting  
 375 the inverse analysis comprised a combination of meta-models and Bayesian interface statistical analysis  
 376 numerical methods. The flow diagram is presented in Figure 11 and detailed as follows.

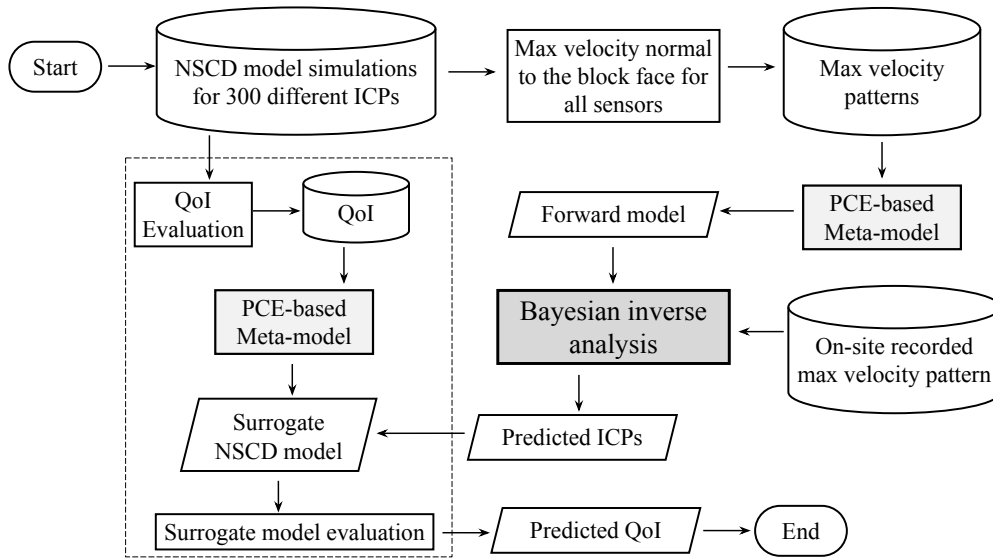


Figure 11: Computational workflow of the inverse analysis using a combination of meta-models, event data and Bayesian inversion methods

377 The rich database of NSCD model simulations for 300 different ICPs (Figure 7) is processed (as per  
 378 Equation 1) to obtain the maximum velocity normal to the block face for all blocks where a sensor is  
 379 planned to be installed. This provides a database of MVP for 300 model computations. This database is

380 processed to create a PCE-based meta-model associating each ICP value set to a distinct MVP.

381 The accuracy of these meta-models is estimated via leave-one-out-error which is estimated of order  
 382  $10^{-2}$  to  $10^{-1}$ . The accuracy of the meta-model representing the MVP, is validated by using the same  
 383 simulation set complemented with an independent set of 300 simulations, for a total of 600 simulations,  
 384 and comparing the predicted vs true value from the NSCD model at all six sensor locations, collectively  
 385 presented in Figure 12.

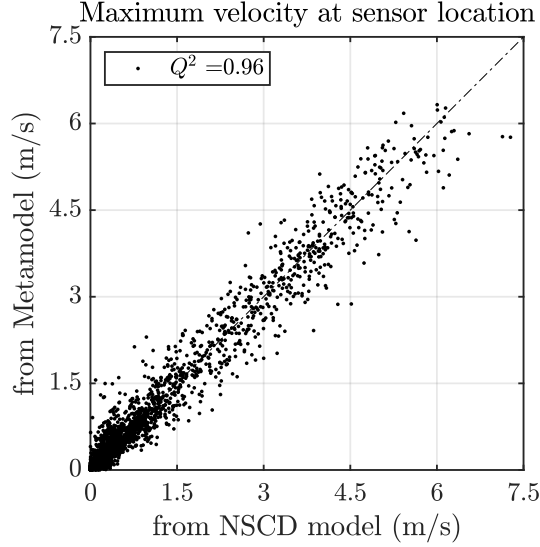


Figure 12: Validation of the PCE-based meta-model of the maximum velocity by comparison of the reported magnitude from 600 NSCD model simulations and the corresponding estimation by the meta-model.

386 The prediction accuracy of the created meta-model is quantified via the predictability coefficient ( $Q^2$ ),  
 387 estimated considering the results from the 600 simulations and 6 points, for a total of 3600 observations,  
 388 as:

$$Q^2 = 1 - \frac{\sum_{i=1}^N (y_i^{\text{pred}} - y_i^{\text{true}})^2}{\sum_{i=1}^N (y_i^{\text{true}} - y_{\text{mean}})^2} \quad (4)$$

389 where  $y_i^{\text{pred}}$  is the meta-model predicted value and  $y_i^{\text{true}}$  is the value processed from the NSCD model  
 390 for block ( $i$ ) and  $y_{\text{mean}}$  is the arithmetic mean of all ‘true’ predictions. The interest of using the meta-  
 391 models is to generalise the maximum concrete block velocity data obtained from 300 (*i.e.*, limited number  
 392 of) simulations, to any possible ICP combination (*i.e.*, a large number), which is a prerequisite for the  
 393 next step.

394 The Bayesian inversion process is deployed where the processed PCE-based meta-model is used as

395 the forward model (or ‘*prior*’, see Equation B.2). This approach is extensively used by many researchers  
 396 (e.g., [35, 36, 16]) to accelerate Bayesian computations. The Bayesian interface is inspired by Bayes’  
 397 theorem [37] - a representation of the changing beliefs - simply demonstrating that the probability of a  
 398 ‘hypothesis’ being correct becomes more reliable with supporting ‘evidence’. In our work, the ‘hypothesis’  
 399 states that the 300 distinct sets of input parameters present a set of 300 distinct MVPs. The idea of  
 400 reliability increase in our hypothesis is that, if we have the on-site recorded MVP as ‘evidence’, then  
 401 there exists at least one set of ICPs (*i.e.*, ‘*posterior*’, see Equation B.3) such that the recorded evidence  
 402 is reproduced. The data obtained from on-site measurements shall provide the MVP which serves as  
 403 evidence for inverse analysis. The Bayesian process estimates the likelihood of this MVP amongst all  
 404 possible MVPs recorded from the meta-models and predicts the corresponding set of ICPs.

405 In the UQlab Bayesian interface framework [38], the uncertainty in the model prediction is assigned  
 406 via added Gaussian discrepancy (see Equation B.5) when correlated with the recorded on-site data. In  
 407 the present work, as the inverse analysis shall rely on a single MVP recorded on-site, deemed less precise,  
 408 the discrepancy with a known residual variance of order  $10^{-3}$  is manually assigned.

409 The output from the Bayesian interface-based inverse analysis is a set of ICP values retrieved as point  
 410 estimates ‘*maximum a posteriori*’ and ‘*mean*’ (see Equation B.13). This predicted set of ICP values is  
 411 then used to estimate the QoI (in this case damage to the wall or distance to the safety line). As a  
 412 conventional approach, running a new NSCD model simulation with the predicted ICPs shall provide  
 413 detailed information on the wall response from which the QoI can be extracted as a subset. However,  
 414 this operation shall require about 30 minutes of computation time and added time for post-processing.  
 415 This added delay time between on-site observation and warning system activation is unfavourable.

416 A procedure by which the QoI is instantly computed is developed to reduce the reaction time. The  
 417 computational workflow components for this process is highlighted in the dashed box of Figure 11. The  
 418 database of NSCD model simulations results is processed to evaluate the QoI as outputs. The resulting  
 419 database of QoI is then used to create the PCE-based meta-model. It serves as a surrogate of the NSCD  
 420 model where the input ICPs are processed to compute the corresponding QoI output. The leave-one-  
 421 out (LOO) error of order  $10^{-2}$  is reported for the two PCE-based meta-models created for the two QoI  
 422 (*i.e.*, distance to safety and wall damage) mentioned above. The predicted ICPs are then fed into this  
 423 surrogate of NSCD model as input which is then evaluated to eventually predict the QoI and the whole

424 computational process terminates.

425 Notably, in the absence of an exhaustive database concerning real structures, the essential ‘evidence’  
426 database (*i.e.*, recorded MVP) to test the inverse analysis process is not available. Therefore, the concrete  
427 block velocity patterns from the same set of 300 model simulations and a new independent set of 300  
428 simulations with different impact conditions are used as pseudo-evidences to test the process.

429 Each of these 600 known block velocity patterns is individually fed as input into the inverse analysis  
430 using the multiple model output feature of Bayesian analysis in UQlab (demonstrated in Equation B.8),  
431 providing the predicted ICP values. The evaluation of the reliability of the inverse analysis is based  
432 on the comparison between the QoI reported via the ICP used for running the simulation, and the one  
433 estimated from evaluating the ICP predicted by the inverse analysis onto the meta-model created for the  
434 same QoI.

#### 435 4.3. Inverse analysis for warning purpose

436 First, the inverse analysis addresses the traffic interruption issue for which the post-impact minimum  
437 distance of the wall to the safety line constitutes the QoI. The higher the distance, the higher the safety.  
438 The predictive capability of the inverse analysis workflow presented in Figure 11 is tested for the maximum  
439 concrete block velocity database obtained from the 600 NSCD model simulations. The MVPs from the  
440 three impact cases mentioned in Section 3.1 are also used to predict the minimum distance to the safety  
441 line.

442 The comparison between the predictions from the inverse analysis + meta-model and the simulation  
443 results is presented in Figure 13. The relative proximity of the predictions to the ideal diagonal reflects  
444 the potential of the presented methodology. Points above the diagonal concern cases for which the inverse  
445 analysis overestimates the distance to the safety line. On the contrary, the inverse analysis underestimates  
446 the distance to the safety lines for points below the diagonal, which is on the safe side.

447 The root mean square (RMS) error of the deviation from the expected response for the 600 simulations  
448 is 16 cm. About 58% of this RMS error is due to the surrogate of the NSCD model (*i.e.*, dashed box  
449 component of the workflow). In fact, in some sectors of the 6D space of the six ICPs, this surrogate  
450 locally fails in precisely capturing the wall response, in particular due to the presence of non-linearities.  
451 As an alternative, the reliability of the inverse analysis could be improved by running an NSCD model  
452 simulation with the predicted ICPs in place of using the surrogate of the NSCD model, at the expense



453 of a longer reaction time upon event.

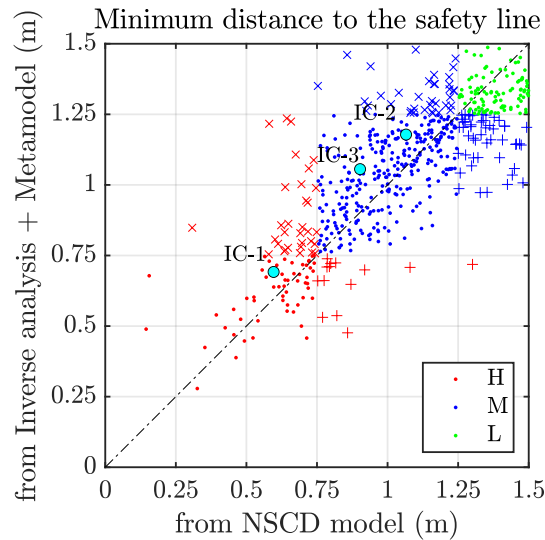


Figure 13: Comparison of the minimum distance from the safety line, estimated from the NSCD model and the corresponding prediction from the inverse analysis tool. Here, the predictions are divided into three zones reflecting high (H), medium (M) and Low (L) levels of severity inclusive of the corresponding zonal false positive (+) and false negative (x) predictions. Results are based on a set of 600 impact conditions complemented with the impact cases presented in section 3.1 (IC-1 to IC-3).

454 For practical purposes, it is proposed to classify the impact response into three classes depending on  
455 the distance to the safety line: [0-0.75 m], [0.75-1.25 m] and [1.25-1.5m]. These classes correspond to  
456 decreasing criticality concerning transport corridor safety, respectively high (H), medium (M) and low  
457 (L) criticality. NSCD model simulation results indicate that 15%, 59% and 26% of the impact cases are  
458 classified in class H, M and L respectively. Predictions based on the inverse analysis + metamodel give  
459 values of 12%, 63% and 25% for classes H, M and L respectively. Besides, the false negative predictions  
460 are estimated to be about 24% and 10% among all in the H and M classes respectively. The remaining  
461 predictions *i.e.*, good and false positives are in favour of the decision-making by the user, and hence are  
462 deemed acceptable.

463 In the end, the predictions are considered sufficiently good to be used in an operational context for  
464 estimating the consequences of the rockfall event in terms of structure displacement. The undeniable  
465 interest in this approach is that it automatically and remotely provides stakeholders with information of  
466 great value for decision-making upon impact. No quantitative evaluation would be derived rapidly from  
467 data measured on-site in the absence of such an approach.

468 4.4. Inverse analysis for structure damage quantification purpose

469 Second, the inverse analysis is used to remotely estimate damage to the wall. It is defined as the  
 470 cumulative energy dissipated by the plasticization of all the wall concrete blocks,  $D_p$ , after the wall is  
 471 at rest. Damage to all concrete blocks of the wall is computed from NSCD model simulations results as  
 472 per section 3.1.4. The approach considered for this inverse analysis is the same as that for the previous  
 473 warning criterion. Figure 14 provides a comparison between  $D_p$  values obtained from NSCD model  
 474 simulations and the predicted ones. The RMS error of the deviation from the expected response is 82 kJ,  
 475 which may be considered acceptable when considering all uncertainties associated with the quantification  
 476 of energy dissipation by plasticization due to real rockfall impacts. Similar to the previous prediction of  
 477 distance, about 35% of the contribution to the RMS error is attributed to the surrogate of the NSCD  
 478 model. Besides, a similar prediction for the three illustrative cases is also presented which reflects a good  
 479 prediction except for the impact at the angled-wedge (*i.e.*, IC-2).

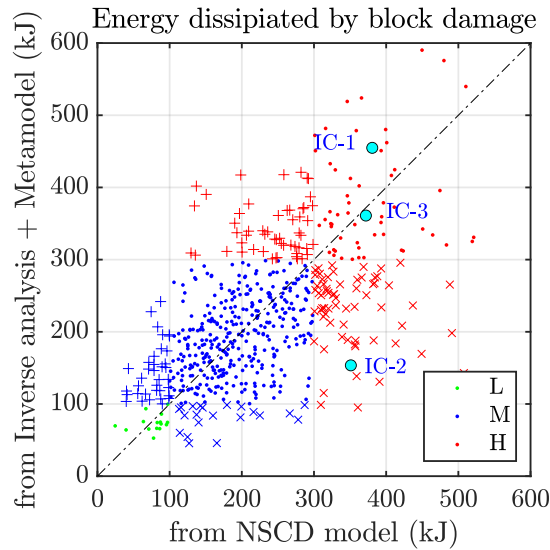


Figure 14: Comparison of the predicted damage to the wall,  $D_p$ , estimated from the NSCD model and the corresponding prediction from the inverse analysis tool. Here, the predictions are divided into three zones reflecting Low (L), medium (M) and high (H) levels of damage inclusive of the corresponding zonal false positive (+) and false negative (x) predictions. Results are based on a set of 600 impact conditions and impact cases presented in section 3.1 (IC-1 to IC-3).

480 The cases in the right upper corner constitute the most critical impact cases. Points above the diagonal  
 481 concern cases for which the inverse analysis overestimates the damage, which is on the safe side. For  
 482 practical purposes, it is proposed to classify the damage into three classes depending on the value of  $D_p$ :  
 483 [0-100 kJ], [100-300 kJ] and [300-800 kJ] for low (L), medium (M) or high (H) damage. These limits were

484 arbitrarily defined from the distribution of  $D_p$  over all cases.

485 The class limits refer to the level of damage to the wall corresponding to the fracture energy of one  
486 concrete block when a fracture propagates along a vertical plane in the middle of the concrete block.  
487 A classification based on the energy dissipation associated with the fracture of the considered concrete  
488 blocks would be more appropriate. Nevertheless, this would require specific and complex tests which are  
489 beyond the scope of the present study. In the absence of specific dynamic test results for these large and  
490 highly reinforced concrete blocks, results obtained by Guo et al. [39] for a reinforced beam exposed to  
491 impact were extrapolated accounting for the difference in block section and resulted in a value of 100 kJ  
492 approx. This value is a rough estimate of the first limit for the considered concrete blocks.

493 According to NSCD model simulations results presented in Figure 14, 8%, 72% and 20% of the impact  
494 cases result in damage classified as H, M and L respectively. Values of 6%, 76% and 18% for classes H, M  
495 and L are obtained from the predictions respectively. Besides, the false negative predictions are estimated  
496 to be about 38% and 5% among all in the H and M classes respectively. The remaining predictions *i.e.*,  
497 good and false positives are in favour of the decision-making by the user, and hence are acceptable.

498 The differences between simulation results and predictions are associated with points at a large dis-  
499 tance from the diagonal (Fig. 14). Further method developments could improve the accuracy of these  
500 predictions. Nevertheless, the predictions following the described inverse analysis are considered suffi-  
501 ciently good to be used in an operational context to aid in remote decision-making, the RMS error is 82  
502 kJ.

#### 503 4.5. Comments concerning the use of inverse analysis based on real-time measurements

504 The results presented in section 4.3 and 4.4 demonstrate the feasibility of conducting an inverse  
505 analysis of data collected on-site during impact, focusing on two specific purposes.

506 The proposed method, making use of numerical modelling, meta-modelling and statistical approaches,  
507 revealed rather efficient in providing useful information which could not be derived from the direct  
508 observation of the data received from the site. The duration of the whole process for treating the input  
509 data typically lasts about five minutes with the developed script making it compatible with rapid reaction  
510 upon event. The analysis scripts are written in Matlab as per UQLab framework [40] allowing running  
511 this complex process in two operations (one for inverse analysis and the other for output of interest  
512 prediction). The accuracy of the predictions is considered sufficiently good for remotely classifying the

513 events and aiding in decision-making. If required for another purpose, this accuracy could be improved  
514 further, for example by also accounting for other measure types, such as inclination, or by improving the  
515 used methodologies for creating the meta-models.

516 In real situations, the probability of occurrence of an impact in given conditions is extremely variable.  
517 By contrast, and as mentioned in section 3.2, the ICP sets considered in this work were defined by not  
518 considering any possible correlation between the various parameters and, more generally, considering that  
519 the ICP sets were equiprobable. The statistical assessment of the inverse analysis predictive capacities is  
520 related to the considered ranges and distributions of the six ICPs. It should thus be considered indicative  
521 at this stage. It should be improved by accounting for the probability of each scenario considered in this  
522 evaluation, for example considering site-specific data describing the rock projectile trajectory.

523 It is worth noting that, as the second step of the inverse analysis provides the set of ICP values  
524 resulting in an MVP similar to the observed one, then a preliminary estimate of the projectile velocity  
525 at impact and consequently the impact energy can also be retrieved complementarily.

## 526 **5. Inverse analysis based on post-impact measurements**

### 527 *5.1. General considerations*

528 In addition to real-time measurements, the wall conformation after impact may be easily obtained by  
529 employing techniques such as photogrammetry or Lidar. Impact-induced displacements with very good  
530 predictions may be obtained if the same type of data is collected before the impact. In such a situation,  
531 the number of data from the site would be much larger than that for real-time response. Typically, the  
532 position of the centre of gravity of all blocks can be derived from these data sets and will be considered  
533 in the following.

534 In this context, the aim of an inverse analysis could be to retrieve information related to the rock  
535 projectile kinematics at impact, such as its kinetic energy. This information could thus contribute to  
536 better quantifying the rockfall hazard at the wall location.

537 The development of the inverse analysis method is based on the following considerations. In case there  
538 is damage to concrete blocks, notably in the impact location vicinity, the determination of the blocks'  
539 gravity centre will not be possible. This eventuality should be accounted for in the development of the  
540 inverse analysis method. In addition, it is considered that the rock projectile volume and the impact

541 location can be determined during the on-site visit. In this process, we assume that the NSCD model  
 542 which is calibrated for a unique projectile mass is also able to predict the structure response for another  
 543 rock projectile mass. In other words, this implies that for a given projectile kinetic energy, the wall  
 544 response is the same whatever the mass and velocity. Under this assumption, the kinetic energy provided  
 545 by the inverse analysis combined with the observed rock projectile mass gives an estimate of its velocity  
 546 at impact.

547 The ICP comprise six physical parameters which describe the projectile kinematics and the point of  
 548 impact on the wall. An accurate prediction of all individual parameters is of limited interest as the user  
 549 is more focused on the estimation of the incident rock projectile kinetic energy. Therefore, it is proposed  
 550 to reduce the dimension of the space of parameters to improve the predictions' reliability. The set of six  
 551 ICPs is reduced to three by combining  $v$ ,  $\Omega$ ,  $\alpha$  and  $\beta$  to calculate the total kinetic energy of the projectile  
 552 ( $KE_{proj}$ ) as per the Equation below and keeping position parameters  $y$  and  $z$  intact.

$$KE_{proj} = \frac{1}{2}m[v_{xy}]^2 + \frac{1}{2}m[v_z]^2 + \frac{1}{2}I[2\pi\Omega]^2 \quad (5)$$

553 Further, the total kinetic energy of the projectile can be divided into two components: one accounting  
 554 for the energy on the plane parallel to the ground ( $KE_p$ ) and the other accounting for the rest of the  
 555 energy ( $KE_{np}$ ). This is done by using only the planer component of the translational velocity ( $v_{xy}$ )  
 556 component to compute  $KE_p$  and the remaining two components (*i.e.*,  $v_z$  and  $\Omega$ ) to compute  $KE_{np}$ .

557 This division is motivated by the observation that  $KE_p$  mainly governs the wall displacement, as it  
 558 is integrally transferred to the wall (except if the projectile rebound velocity is significant, which is not  
 559 the case here). On the contrary, the rest of the energy (which is associated with projectile rotation and  
 560 velocity along the vertical direction) is marginally transferred to the wall and thus has very little influence  
 561 on the wall response.

562 This proposition is qualitatively explored by the Sobol indices evaluated on reduced ICPs for the  
 563 maximum 3D displacement, presented in Figure 15. Here,  $KE_p$  is observed highly influential for the  
 564 resulting maximum displacement of the wall and as suspected,  $KE_{np}$  provides negligible influence. The  
 565 y-position of the projectile impact is observed as influential and supports the conclusion presented in the  
 566 previous section. The position-z is observed to have a negligible influence which supports the conclusions  
 567 in the previous section as well. Thereby, observing from the Sobol indices, the inverse analysis is conducted

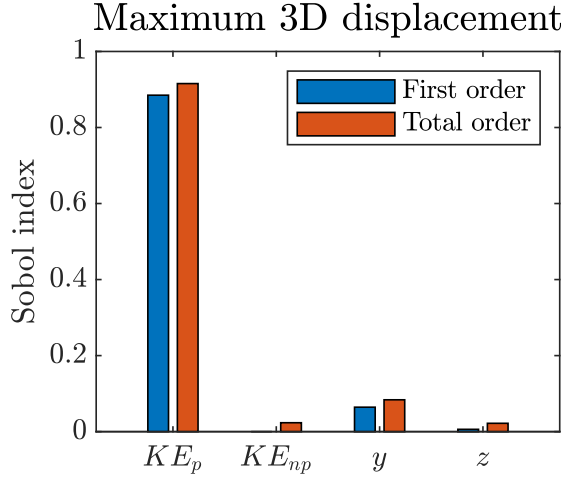


Figure 15: Sobol sensitivity analysis of the impact condition parameters (ICPs) of derived and reduced dimensions (*i.e.*, from 6 to 4) for the maximum 3D displacement

568 taking into account the variability in the  $KE_p$  and  $y$  parameters only hereby referred to as reduced  
 569 dimension ICPs.

### 570 5.2. Inverse analysis method

571 The process of inverse analysis for displacement-based prediction of the impact conditions follows  
 572 nearly the same workflow as presented in the previous section and illustrated in Figure 11. Here, the set  
 573 of 300 simulations is processed to generate the meta-model of the pattern of the displacement at rest of  
 574 the gravity centre of all blocks (similar to the MVP).

575 The accuracy of the created meta-model was estimated of order  $10^{-1}$  via leave-one-out-error. Be-  
 576 sides, the created meta-model for 3D displacement is validated by using the same simulation set and an  
 577 independent set of 300 simulations (thus a total of 600 simulations) and comparing the predicted vs true  
 578 value (from NSCD model) at all 26 blocks in the movement zone, collectively presented in Figure 16.  
 579 Here, the predictability coefficient ( $Q^2$ ) presents the prediction accuracy, estimated for  $N = 600 \times 26 =$   
 580 15600 observations as per Equation 4.

581 This created meta-model is used as a forward model for the Bayesian interface-based inverse analysis.  
 582 The displacement data retrieved from real events shall serve as evidence for the inverse analysis, similar to  
 583 the ‘on-site MVP’ mentioned in the previous section. Notably, here, two threshold levels of displacement  
 584 magnitude are set at 0.2m and 0.05m for the recorded data from all 26 blocks. The first threshold of  
 585 0.2m is assigned to limit the number of blocks in the displacement pattern to avoid overfitting. The

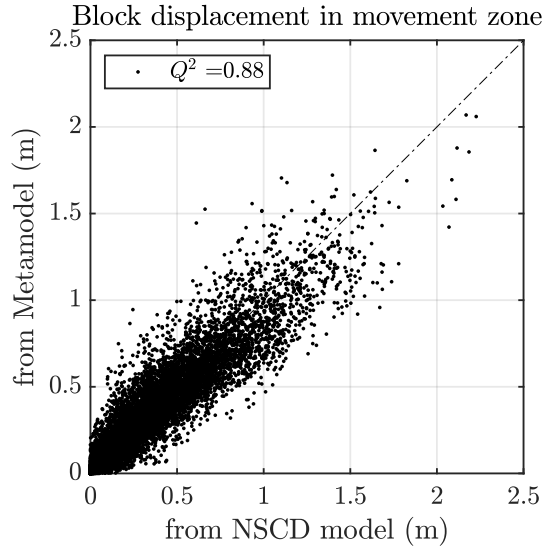


Figure 16: Validation of PCE-based meta-model of the 3D displacement of 26 blocks by comparison of the reported magnitude from 600 NSCD model simulations and the corresponding estimation by the meta-model

586 second threshold of 0.05m is assigned to take into account a sufficient number of blocks for a small wall  
 587 displacement situation where the first threshold limits the total number of moving blocks to maximum  
 588 three.

589 The corresponding reduced dimension ICPs are predicted and the inverse analysis process terminates.  
 590 Notably, the workflow corresponding to the evaluation of the QoI and the associated process to create a  
 591 meta-model serving as a surrogate of the NSCD model is therefore not required.

### 592 5.3. Evaluation of the method

593 Following the guidelines of the previous section, the predictions of the energy transferred to the wall  
 594 and the position of impact are compared with the corresponding NSCD model simulation results. These  
 595 comparisons are presented in Figure 17 for the simulated 600 distinct impact conditions and the three  
 596 illustrative impact conditions.

597 The energy transferred to the wall is predicted with an overall RMS error of 71 kJ (which is below the  
 598 fracture energy of the concrete block) based on 600 simulations. The overall prediction is satisfactory for  
 599 a wide range of energy magnitudes supporting the potential of the presented methodology. Nevertheless,  
 600 two out of three illustrative cases are badly predicted with up to 120 kJ difference from the expected  
 601 520kJ for all cases (IC-1 and IC-3).

602 Further, the position of impact along the wall length is rather well predicted for impacts at convex  
 603 and concave-wedges, including the illustrative impact tests in these two locations (IC-1 and IC-3). By

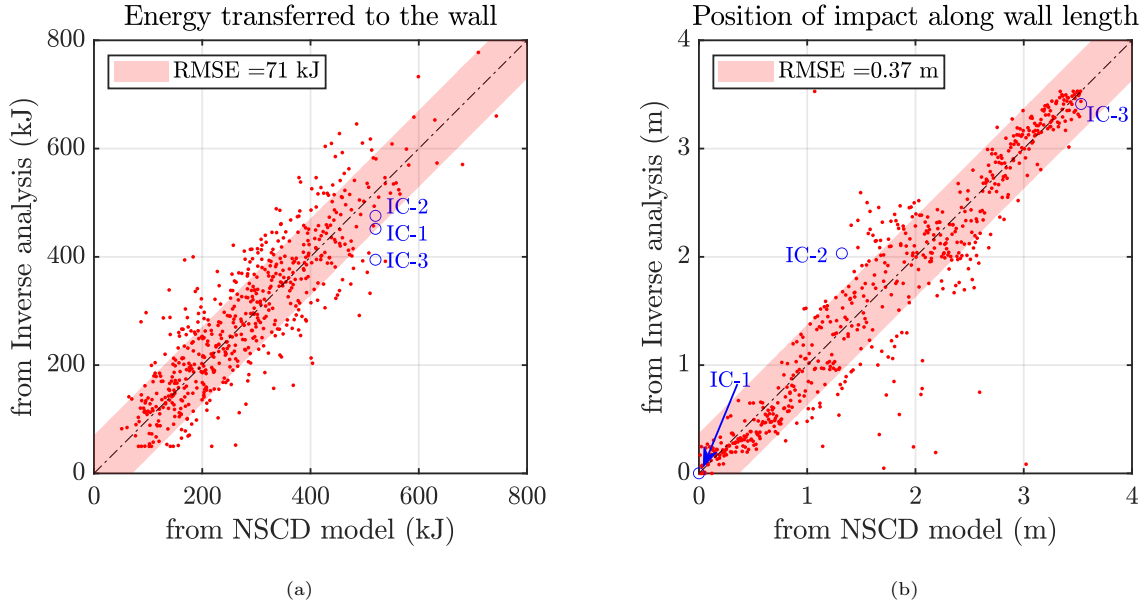


Figure 17: Comparison of displacement-scan inverse analysis-based predictions of (a) energy transferred to the wall and (b) position along the wall length with the corresponding magnitude deduced from 600 different sets of the impact condition parameters.

604 contrast, the predictions for the angled wedge zone (between 1.2 to 2.2 m approx.) are significantly  
 605 less accurate thereby contributing to the overall RMS error of 37 cm. This significant difference in  
 606 predictions accuracy is attributed to the zig-zag conformation of the wall, which amplifies the influence  
 607 of the deviation angle ( $\beta$ ) on the structure response depending on the impact location, as illustrated  
 608 by the Sobol indices. In fact, considering a reduced ICPs input space dimension suppresses the distinct  
 609 contribution of  $\beta$  which in turn suppresses the variability of the impact at the angled wedge.

## 610 6. Conclusions

611 This work explored the potential of inverse analysis to obtain the information of interest in the  
 612 operational context of a rockfall protection structure. The inverse analysis relies on simulation-based  
 613 predictions of the structure response and makes use of the Bayesian interface and meta-modelling tech-  
 614 niques. This work in particular focuses on rockfall protection walls made of piled-up and articulated  
 615 concrete blocks for which an NSCD model was previously developed and calibrated against real-scale  
 616 impact experiments.

617 The main conclusions drawn from this research are :

- 618 • Provided a well-calibrated model is available, it is possible to carry out reliable inverse analysis of



619 the response of complex structures subjected to localised dynamic loading.

- 620 • Investigating the structure response considering a wide range of impact conditions, representative  
621 of those encountered in situ is a prerequisite in view of defining the strategy for developing the  
622 inverse analysis method.
- 623 • The inverse analysis may be based on real-time or post-impact measurements and may serve various  
624 purposes, in particular for remote warning upon impact or rockfall activity survey.
- 625 • The presented inverse analysis framework is transferable to other types of such structures (such as  
626 flexible barriers) via the usage of the relevant recorded database.

627 As a perspective, the accuracy of the predictions by the inverse analysis will be improved, focusing  
628 on the meta-models which are key components in the proposed method. As a supplementary outcome,  
629 the recorded concrete block velocity database for different impact conditions can be further exploited  
630 towards the optimisation of the sensor location.

## 631 **References**

- 632 [1] S. Lambert, F. Bourrier, Design of rockfall protection embankments: A review, *Engineering Geology*  
633 154 (2013) 77–88.
- 634 [2] F. Calvetti, Rockfall shelters covered by granular layers, *European Journal of Environmental and*  
635 *Civil Engineering* (2011).
- 636 [3] C. Gentilini, G. Gottardi, L. Govoni, A. Mentani, F. Ubertini, Design of falling rock protection  
637 barriers using numerical models, *Engineering Structures* 50 (2013) 96–106. *Engineering Structures:*  
638 *Modelling and Computations* (special issue IASS-IACM 2012).
- 639 [4] F. Bourrier, J. Baroth, S. Lambert, Accounting for the variability of rock detachment conditions in  
640 designing rockfall protection structures, *Natural Hazards* (2016).
- 641 [5] A. Segalini, A. Valletta, A. Carri, R. Savi, Impact identification on flexible rockfall barriers: on site  
642 test of a wireless monitoring system, *IOP Conference Series: Earth and Environmental Science* 1124  
643 (2023) 012125.

- 644 [6] M. Ragnoli, A. Leoni, G. Barile, G. Ferri, V. Stornelli, Lora-based wireless sensors network for  
645 rockfall and landslide monitoring: A case study in pantelleria island with portable lorawan access,  
646 J. Low Power Electron. Appl. 12 (2022).
- 647 [7] P. Mayer, R. Rogge, A. Caviezel, J. Munch, A. Ringenbach, M. Magno, L. Benini, Design and  
648 evaluation of a lora controlled rugged multisensor unit for induced rockfall experiments, in: 2023  
649 9th International Workshop on Advances in Sensors and Interfaces (IWASI), 2023, pp. 52–57. doi:[10.1109/IWASI58316.2023.10164375](https://doi.org/10.1109/IWASI58316.2023.10164375).  
650
- 651 [8] L. Castanon-Jano, E. Blanco-Fernandez, D. Castro-Fresno, D. Ferreño, Use of explicit fem models  
652 for the structural and parametrical analysis of rockfall protection barriers, Engineering Structures  
653 (2018).
- 654 [9] L. Dugelas, J. B. Coulibaly, F. Bourrier, S. Lambert, M.-A. Chanut, I. Olmedo, F. Nicot, Assessment  
655 of the predictive capabilities of discrete element models for flexible rockfall barriers, International  
656 Journal of Impact Engineering 133 (2019) 103365.
- 657 [10] Z.-H. Zhu, J.-H. Yin, J.-Q. Qin, D.-Y. Tan, A new discrete element model for simulating a flexible ring  
658 net barrier under rockfall impact comparing with large-scale physical model test data, Computers  
659 and Geotechnics (2019).
- 660 [11] J. P. Hambleton, O. Buzzi, A. Giacomini, M. Spadari, S. W. Sloan, Perforation of flexible rockfall  
661 barriers by normal block impact, Rock Mechanics and Rock Engineering (2013).
- 662 [12] Z. Yu, L. Luo, C. Liu, L. Guo, X. Qi, L. Zhao, Dynamic response of flexible rockfall barriers with  
663 different block shapes, Landslides (2021).
- 664 [13] A. Mentani, L. Govoni, G. Gottardi, S. Lambert, F. Bourrier, D. Toe, A new approach to evaluate  
665 the effectiveness of rockfall barriers, Procedia Engineering 158 (2016) 398–403. VI Italian Conference  
666 of Researchers in Geotechnical Engineering, CNRIG2016 - Geotechnical Engineering in Multidisci-  
667 plinary Research: from Microscale to Regional Scale, 22-23 September 2016, Bologna (Italy).
- 668 [14] S. Lambert, D. Toe, A. Mentani, F. Bourrier, A Meta-Model-Based Procedure for Quantifying the  
669 On-Site Efficiency of Rockfall Barriers, Rock Mechanics and Rock Engineering 54 (2021) 487–500.

- 670 [15] J. Escallón, C. Wendeler, E. Chatzi, P. Bartelt, Parameter identification of rockfall protection barrier  
671 components through an inverse formulation, *Engineering Structures* 77 (2014) 1–16.
- 672 [16] R. Gupta, F. Bourrier, V. Acary, S. Lambert, Bayesian interface based calibration of a novel  
673 rockfall protection structure modelled in the non-smooth contact dynamics framework, *Engineering*  
674 *structures* 297 (2023).
- 675 [17] A. Furet, S. Lambert, P. Villard, J. P. Jarrin, Experimental and numerical impact responses of an  
676 innovative rockfall protection structure made of articulated concrete blocks, *Rock Mechanics and*  
677 *Rock Engineering* (2022).
- 678 [18] S. Lambert, F. Bourrier, P. Gotteland, F. Nicot, An experimental investigation of the response of  
679 slender protective structures to rockfall impacts, *Canadian geotechnical journal* (2019).
- 680 [19] O. Korini, M. Bost, J.-P. Rajot, Y. Bennani, N. Freitag, The influence of geosynthetics design on the  
681 behavior of reinforced soil embankments subjected to rockfall impacts, *Engineering Geology* (2021).
- 682 [20] EOTA, Ead 340059-00-0106: Falling rock protections kits, 2018.
- 683 [21] V. Acary, F. Perignon, Siconos: A Software Platform for Modeling, Simulation, Analysis and Control  
684 of Nonsmooth Dynamical Systems, *SIMULATION NEWS EUROPE*, ArgeSIM/ASIM 17 (2007) 19–  
685 26.
- 686 [22] V. Acary, Energy conservation and dissipation properties of time-integration methods for nonsmooth  
687 elastodynamics with contact, *ZAMM - Journal of Applied Mathematics and Mechanics / Zeitschrift*  
688 *für Angewandte Mathematik und Mechanik* 96 (2016) 585–603.
- 689 [23] S. Lambert, R. Gupta, F. Bourrier, V. Acary, What can we learn from simulation-based quantifi-  
690 cation of energy dissipation in rockfall protection structures? case of an articulated wall modelled  
691 with the nscd method, *Rock Mechanics and Rock Engineering* (submitted).
- 692 [24] D. Toe, A. Mentani, L. Govoni, F. Bourrier, G. Gottardi, S. Lambert, Introducing meta-models for  
693 a more efficient hazard mitigation strategy with rockfall protection barriers, *Rock Mechanics and*  
694 *Rock Engineering* 51 (2018) 1097–1109.
- 695 [25] M. Previtali, M. O. Ciantia, S. Spadea, R. Castellanza, G. Crosta, Assessing rockfall barrier perfor-  
696 mance through block propagation codes and meta-models, in: M. Barla, A. Di Donna, D. Sterpi,

- 697 A. Insana (Eds.), Challenges and Innovations in Geomechanics, Springer International Publishing,  
698 Cham, 2023, pp. 291–298.
- 699 [26] F. Bourrier, F. Berger, P. Tardif, L. Dorren, O. Hungr, Rockfall rebound: comparison of detailed  
700 field experiments and alternative modelling approaches, *Earth Surface Processes and Landforms* 37  
701 (2012) 656–665.
- 702 [27] M. Spadari, A. Giacomini, O. Buzzi, J. Hambleton, Prediction of the bullet effect for rockfall barriers:  
703 a scaling approach, *Rock Mechanics and Rock Engineering* (2012).
- 704 [28] A. Breugnot, S. Lambert, P. Villard, P. Gotteland, A discrete/continuous coupled approach for  
705 modeling impacts on cellular geostructures, *Rock Mechanics and Rock Engineering* (2016).
- 706 [29] C. Lataniotis, S. Marelli, B. Sudret, UQLab user manual – The Input module, Technical Report,  
707 Chair of Risk, Safety & Uncertainty Quantification, ETH Zurich, 2015. Report UQLab-V0.9-102.
- 708 [30] I. M. Sobol, A screening design for factorial experiments with interactions, *Mathematical and*  
709 *Computer Modelling* 1 (1993) 407–414.
- 710 [31] B. Sudret, Global sensitivity analysis using polynomial chaos expansions, *Reliability Engineering &*  
711 *System Safety* 93 (2008) 964–979. Bayesian Networks in Dependability.
- 712 [32] E. Rouzies, C. Lauvernet, B. Sudret, A. Vidard, How is a global sensitivity analysis of a catchment-  
713 scale, distributed pesticide transfer model performed? application to the peshmelba model, *Geosci-*  
714 *entific Model Development* 16 (2023) 3137–3163.
- 715 [33] S. Marelli, B. Sudret, Uqlab user manual - polynomial chaos expansions, 2015. doi:[10.13140/RG.2.](https://doi.org/10.13140/RG.2.1.3778.7366)  
716 [1.3778.7366](https://doi.org/10.13140/RG.2.1.3778.7366).
- 717 [34] S. Marelli, C. Lamas, K. Konakli, C. Mylonas, P. Wiederkehr, B. Sudret, UQLab user manual –  
718 Sensitivity analysis, Technical Report, Chair of Risk, Safety and Uncertainty Quantification, ETH  
719 Zurich, Switzerland, 2022. Report UQLab-V2.0-106.
- 720 [35] M. A. Hariri-Ardebili, B. Sudret, Polynomial chaos expansion for uncertainty quantification of dam  
721 engineering problems, *Engineering Structures* 203 (2020) 109631.
- 722 [36] X. Guo, D. Dias, C. Carvajal, L. Peyras, P. Breul, Reliability analysis of embankment dam sliding  
723 stability using the sparse polynomial chaos expansion, *Engineering Structures* 174 (2018) 295–307.

724 [37] T. Bayes, N. Price, LII. An essay towards solving a problem in the doctrine of chances. by the late  
 725 Rev. Mr. Bayes, F. R. S. communicated by Mr. Price, in a letter to John Canton, A. M. F. R. S.,  
 726 Philosophical Transactions of the Royal Society of London 53 (1763) 370–418.

727 [38] P.-R. Wagner, J. Nagel, S. Marelli, B. Sudret, UQLab user manual – Bayesian inversion for model  
 728 calibration and validation, Technical Report, Chair of Risk, Safety and Uncertainty Quantification,  
 729 ETH Zurich, Switzerland, 2022. Report UQLab-V2.0-113.

730 [39] J. Guo, J. Cai, Q. Chen, X. Liu, Y. Wang, Z. Zuo, Dynamic behaviour and energy dissipation of  
 731 reinforced recycled aggregate concrete beams under impact, Construction and Building Materials  
 732 (2019).

733 [40] S. Marelli, B. Sudret, UQLab: A Framework for Uncertainty Quantification in Matlab, 2014, pp.  
 734 2554–2563. doi:[10.1061/9780784413609.257](https://doi.org/10.1061/9780784413609.257).

## 735 Appendix A. PCE based meta-model

736 Consider the articulated structure model represented by a  $\mathcal{M}(\mathbf{X})$  as an equivalent mathematical  
 737 model. Here,  $\mathbf{X} \in \mathbb{R}^M$  is a random vector with independent components described by the joint probability  
 738 density function (PDF)  $f_{\mathbf{X}}$ . Consider also a finite variance computational model as a map  $Y = \mathcal{M}(\mathbf{X})$ ,  
 739 with  $Y \in \mathbb{R}$  such that:

$$\mathbb{E} [Y^2] = \int_{\mathcal{D}_{\mathbf{X}}} \mathcal{M}(\mathbf{x})^2 f_{\mathbf{X}}(\mathbf{x}) d\mathbf{x} < \infty \quad (\text{A.1})$$

740 Then, under the assumption of Equation A.1, the PCE of  $\mathcal{M}(\mathbf{X})$  is defined as:

$$Y = \mathcal{M}(\mathbf{X}) = \sum_{\alpha \in \mathbb{N}^M} y_{\alpha} \Psi_{\alpha}(\mathbf{X}) \quad (\text{A.2})$$

741 where, the  $\Psi_{\alpha}(\mathbf{X})$  are multivariate polynomials orthonormal with respect to  $f_{\mathbf{X}}$ ,  $\alpha \in \mathbb{N}^M$  is a multi-  
 742 index that identifies the components of the multivariate polynomials  $\Psi_{\alpha}$  and the  $y_{\alpha} \in \mathbb{R}$  are the corre-  
 743 sponding coefficients. In practical applications, the sum in Equation A.2 needs to be truncated to a finite  
 744 sum by introducing the truncated polynomial chaos expansion:

$$\mathcal{M}(\mathbf{X}) \approx \mathcal{M}^{PC}(\mathbf{X}) = \sum_{\alpha \in \mathcal{A}} y_{\alpha} \Psi_{\alpha}(\mathbf{X}) \quad (\text{A.3})$$

745 where,  $\mathcal{A} \subset \mathbb{N}^M$  is the set of selected multi-indices of multivariate polynomials.

746 In this work, the least-angle regression (LARS) method is used to create the PCE meta-model trun-  
 747 cated to the maximum polynomial degree ( $p$ ) ranging from 1 to 20, and using hyperbolic truncation  
 748 scheme ( $q$ ) ranging from 0.5 to 1.

$$\mathcal{A}^{M,p,q} = \{\boldsymbol{\alpha} \in \mathcal{A}^{M,p} : \|\boldsymbol{\alpha}\|_q \leq p\}, \text{ where } \|\boldsymbol{\alpha}\|_q = \left( \sum_{i=1}^M \alpha_i^q \right)^{1/q} \quad (\text{A.4})$$

749 The accuracy of the constructed PCE is estimated by computing the leave-one-out (LOO) cross-  
 750 validation error ( $\epsilon_{LOO}$ ). It consists in building  $N$  meta-models  $\mathcal{M}^{PC \setminus i}$ , each one created on a reduced  
 751 experimental design  $\mathfrak{X} \setminus \mathbf{x}^{(i)} = \{\mathbf{x}^{(j)}, j = 1, \dots, N, j \neq i\}$  and comparing its prediction on the excluded  
 752 point  $\mathbf{x}^{(i)}$  with the real value  $y^{(i)} = \mathcal{M}(\mathbf{x}^{(i)})$  [33]. The leave-one-cross-validation error can be written as:

$$\epsilon_{LOO} = \frac{\sum_{i=1}^N \left( \mathcal{M}(\mathbf{x}^{(i)}) - \mathcal{M}^{PC \setminus i}(\mathbf{x}^{(i)}) \right)^2}{\sum_{i=1}^N \left( \mathcal{M}(\mathbf{x}^{(i)}) - \hat{\mu}_Y \right)^2} \quad (\text{A.5})$$

753 where,  $\hat{\mu}_Y$  is the mean of the experimental design sample.

## 754 Appendix B. Bayesian interface for inverse analysis

755 Consider the computational model  $\mathcal{M}$  that allows the analyst to predict certain quantities of interest  
 756 gathered in a vector  $\mathbf{y} \in \mathbb{R}^{N_{out}}$  as a function of input parameters  $\mathbf{x}$ :

$$\mathcal{M} : \mathbf{x} \in \mathcal{D}_{\mathbf{X}} \subset \mathbb{R}^M \mapsto \mathbf{y} = \mathcal{M}(\mathbf{x}) \in \mathbb{R}^{N_{out}} \quad (\text{B.1})$$

757 The Bayesian interface for inverse analysis focuses on identifying the input parameters of a computa-  
 758 tional model to recover the observations in the collected output data set. It comprises of a computational  
 759 forward model  $\mathcal{M}$ , a set of input parameters  $\mathbf{x} \in \mathcal{D}_{\mathbf{X}}$  that need to be inferred, and a set of experimental  
 760 data  $\mathcal{Y}$ . Here,  $\mathcal{Y} \stackrel{\text{def}}{=} \{\mathbf{y}_1, \dots, \mathbf{y}_N\}$  is a global data set of  $N$  independent measured quantities of interest  
 761 ( $\mathbf{y}_i$ ).

762 The forward model  $\mathbf{x} \mapsto \mathcal{M}(\mathbf{x})$  is a mathematical representation of the system under consideration.  
 763 The lack of knowledge on the input parameters is modelled by considering them as a random vector,  
 764 denoted by  $\mathbf{X}$  which is assumed to follow a so-called prior distribution (with support  $\mathcal{D}_{\mathbf{X}}$ ), as presented  
 765 in Figure 7 in the present work.

$$\mathbf{X} \sim \pi(\mathbf{x}) \tag{B.2}$$

766 The Bayesian statistics combine this prior knowledge of the parameters with the few observed data  
 767 points to obtain a statistical model called posterior distribution ( $\pi(\mathbf{x} | \mathbf{y})$ ) of the input parameters, using  
 768 Bayes' theorem [37], expressed as:

$$\pi(\mathbf{x} | \mathbf{y}) = \frac{\pi(\mathbf{y} | \mathbf{x})\pi(\mathbf{x})}{\pi(\mathbf{y})} \tag{B.3}$$

769 Now, considering the available data set ( $\mathcal{Y}$ ) as independent realizations of  $\mathbf{Y} | \mathbf{x} \sim \pi(\mathbf{y} | \mathbf{x})$ , the  
 770 collected measurements result in the definition of the likelihood function  $\mathcal{L}(\mathbf{x}; \mathcal{Y})$ , which is a function of  
 771 input parameters  $\mathbf{x}$ :

$$\mathcal{L} : \mathbf{x} \mapsto \mathcal{L}(\mathbf{x}; \mathcal{Y}) \stackrel{\text{def}}{=} \prod_{i=1}^N \pi(\mathbf{y}_i | \mathbf{x}) \tag{B.4}$$

772 This implicitly assumes in/dependence between individual measurements in  $\mathcal{Y}$ . Intuitively the like-  
 773 lihood function for a given  $\mathbf{x}$  returns the relative likelihood of observing the data at hand, under the  
 774 assumption that it follows the prescribed parametric distribution  $\pi(\mathbf{y} | \mathbf{x})$ .

775 As all models are simplifications of the real world, a discrepancy term ( $\epsilon$ ) is introduced to connect  
 776 real-world observations ( $\mathcal{Y}$ ) to the predictions by the model. In practice, the discrepancy term represents  
 777 the effects of the measurement error and model inaccuracy. The discrepancy term introduced here reads:

$$\mathbf{y} = \mathcal{M}(x) + \epsilon \tag{B.5}$$

778 Here, the  $\epsilon$  is assumed as an additive Gaussian discrepancy [38] with a zero mean and given covariance  
 779 matrix ( $\mathbf{\Sigma}$ ):

$$\epsilon \sim \mathcal{N}(\epsilon | \mathbf{0}, \mathbf{\Sigma}) \tag{B.6}$$

780 Taking insights from the discrepancy term definition, a particular measurement point ( $\mathbf{y}_i \in \mathcal{Y}$ , is a  
 781 realization of the Gaussian distribution with mean value  $\mathcal{M}(x)$  and covariance matrix  $\mathbf{\Sigma}$ . This distribution  
 782 is named as discrepancy model and is expressed as:

$$\pi(\mathbf{y} | \mathbf{x}) = \mathcal{N}(\mathbf{y} | \mathcal{M}(\mathbf{x}), \mathbf{\Sigma}) \tag{B.7}$$

783 In application, the discrepancy model defines the connection between the supplied data ( $\mathcal{Y}$ ) and  
784 the forward model. In the present work, as the inverse analysis is conducted on the pseudo on-site  
785 measurement (as evidence), the discrepancy model with known residual variance is assigned.

786 Afterwards, the  $N$  independent available measurements (in our case, maximum velocity pattern and  
787 3D displacement databases) gathered in the data-set (*i.e.*,  $\mathcal{Y} = \{\mathbf{y}_1, \dots, \mathbf{y}_N\}$ ) are used to define the  
788 likelihood function as:

$$\begin{aligned} \mathcal{L}(\mathbf{x}; \mathcal{Y}) &= \prod_{i=1}^N \mathcal{N}(\mathbf{y}_i | \mathcal{M}(\mathbf{x}), \Sigma) \\ &= \prod_{i=1}^N \frac{1}{\sqrt{(2\pi)^{N_{out}} \det(\Sigma)}} \exp\left(-\frac{1}{2}(\mathbf{y}_i - \mathcal{M}(\mathbf{x}))^\top \Sigma^{-1}(\mathbf{y}_i - \mathcal{M}(\mathbf{x}))\right) \end{aligned} \quad (\text{B.8})$$

789 Thereby, following Bayes' theorem, the posterior distribution  $\pi(\mathbf{x} | \mathcal{Y})$  of the parameters ( $\mathbf{x}$ ) given  
790 the observations in  $\mathcal{Y}$  can be written as:

$$\pi(\mathbf{x} | \mathcal{Y}) = \frac{\mathcal{L}(\mathbf{x}; \mathcal{Y})\pi(\mathbf{x})}{Z} \quad (\text{B.9})$$

791 Here,  $Z$  is a normalizing factor, known as the marginal likelihood or evidence, is added to ensure that  
792 this distribution integrates to 1:

$$Z \stackrel{\text{def}}{=} \int_{\mathcal{D}_{\mathbf{x}}} \mathcal{L}(\mathbf{x}; \mathcal{Y})\pi(\mathbf{x})d\mathbf{x} \quad (\text{B.10})$$

793 The closed-form solutions do not exist in practice, and therefore the posterior distribution is obtained  
794 through Markov chain Monte Carlo (MCMC) simulations. In the present work, among many proposed  
795 algorithms in [38], the Adaptive Metropolis (AM) algorithm is used and 100 parallel chains with 1000  
796 steps are assigned to the MCMC solver. The start of the covariance adaptation in AM algorithm is  
797 assigned at the 100th step (see Wagner et al. [38] for more details).

798 The output ( $\mathbf{y}$ ) predictive capabilities of the Bayesian interface is assessed through the comparison of  
799 prior ( $\pi(\mathbf{y})$ ) and posterior ( $\pi(\mathbf{y} | \mathcal{Y})$ ) output distributions as:

$$\pi(\mathbf{y}) = \int_{\mathcal{D}_{\mathbf{x}}} \pi(\mathbf{y} | \mathbf{x})\pi(\mathbf{x})d\mathbf{x} \quad (\text{B.11})$$

$$\pi(\mathbf{y} | \mathcal{Y}) = \int_{\mathcal{D}_{\mathbf{x}}} \pi(\mathbf{y} | \mathbf{x})\pi(\mathbf{x} | \mathcal{Y})d\mathbf{x} \quad (\text{B.12})$$



800 Lastly, in the present studies, the purpose of the Bayesian interface is to obtain the ‘best set of impact  
801 condition parameters (ICPs)’. Given the posterior distribution ( $\pi(\mathbf{x} | \mathcal{Y})$ ), we are interested in finding a  
802 suitable set among the posterior computed set *i.e.*,  $\mathbf{X} | \mathcal{Y}$ . This is done through a point estimator ( $\hat{\mathbf{x}}$ )  
803 computed from:

$$\pi(\mathbf{y} | \mathcal{Y}) \stackrel{\text{def}}{=} \pi(\mathbf{y} | \hat{\mathbf{x}}) \tag{B.13}$$

804 This point estimator can be a mean or mode (maximum a posteriori ‘MAP’) [38] of the posterior  
805 distribution as per the user’s choice.